Decoupling wing-shape effects of wing-swept angle and aspect ratio on a forward-flying butterfly

Sheng-Kai Chang, You-Jun Lin, Kuan-Lun Hsu,[*] and Jing-Tang Yang[†]

Department of Mechanical Engineering, National Taiwan University, Taipei 106319, Taiwan

The effect of wing shape on a forward-flying butterfly via decoupled factors of the wing-swept angle and the aspect ratio (AR) was investigated numerically. The wing-shape effect is a major concern in the design of a microaerial vehicle (MAV). In nature, the wing of a butterfly consists of partially overlapping forewing and hindwing; when the forewing sweeps forward or backward relative to the hindwing, the wing-swept angle and the AR of the entire wing simultaneously change. The effects of the wing-swept angle and AR on aerodynamics are coupled. To decouple their effects, we established wing-shape models with varied combinations of the wing-swept angle and AR based on the experimental measurement of two butterfly species (*Papilio polytes* and *Kallima inachus*) and developed a numerical simulation for analysis. In each model, the forewing and hindwing overlapped partially, constructing a single wing. Across the models, the wing-swept angle and AR of these single wings varied sequentially. The results show that, through our models, the effects of the wing-swept angle and AR were decoupled; both have distinct flow mechanisms and aerodynamic force trends and are consistent in the two butterfly species. For a fixed AR, a backward-swept wing increases lift and drag because of the enhanced attachment of the leading-edge vortex with increased strength of the wingtip vortex and the spanwise flow. For a fixed wing-swept angle, a small AR wing increases lift and decreases drag because of the large region of low pressure downstream and the wake-capture effect. Coupling these effects, the largest lift-to-drag ratio occurs for a forward-swept wing with the smallest AR. These results indicate that, in a flapping forward flight, sweeping a forewing forward relative to a hindwing is suitable for cruising. The flow mechanisms and decoupled and coupled effects of the wing-swept angle and the AR presented in this paper provide insight into the flight of a butterfly and the design of a MAV.

I. INTRODUCTION

The flight of insects has aroused much attention among biophysicists and the public in recent years. Through ~400 million years of evolution, insects have surmounted natural selection and have developed sophisticated flying techniques involving flapping wings. They can immediately take off, hover, or even fly reversely. Such astonishing flight techniques in insects, which are incomparable with traditional aircraft, has inspired humans to create microaerial vehicles (MAVs). A MAV is defined as an aircraft of size <15 cm and flight speed up to 15 m s^{-1} and is designed to serve in surveillance, rescue, or exploration over extreme terrain [1,2]. Understanding the mechanism of insect flight and its correlation with the insect morphology has become a primary objective of aerodynamic research.

Among insects of multiple kinds, butterflies utilize a unique wing-shape control method to fly. Morphologically, a butterfly has four wings, two wings on each side; during flapping, the forewing and hindwing on each side overlap partially, constructing a single, broad, and short wing [3–10]. Experimental measurements have shown that, during flight,

a butterfly changes its wing shape by sweeping the forewing forward and backward relative to the hindwing [11–13]. This forewing-sweeping motion affects not only the wing-swept angle but also the aspect ratio (AR) of the entire wing, which are the two important geometric parameters to affect flight [14,15]. Figure 1 presents a schematic of the forewing-sweeping motion. The wing-swept angle (η) is defined as an angle between the line connecting a wingtip and a wing root and the right-hand-side vector of the body. The AR is a ratio of a wingspan (b) to a mean chord ($\bar{c}$), of which the mean chord is the wing surface area divided by the wingspan. As the forewing sweeps forward, the wing-swept angle increases, and the AR of the entire wing decreases, and vice versa (Fig. 1). This condition indicates that, via the forewing-sweeping motion, the effects of the wing-swept angle and AR on aerodynamics are coupled.

Although a butterfly can use the forewing-sweeping motion to change the wing-swept angle and AR, the mechanism of how the forewing-sweeping motion affects flight was not thoroughly clarified. There is no single relation between the forewing-sweeping motion and the flight in the literature. Fujikawa *et al.* [11] measured a taking-off butterfly (*Papilio xuthus*) and indicated that the forewing sweeps at middownstroke and midupstroke, whereas Sunada *et al.* [12] reported that the forewing of a taking-off butterfly (*Pieris melete*) sweeps at the early stage of a downstroke. For forward flight,

---
[*]Corresponding author: kuanlunhsu@ntu.edu.tw
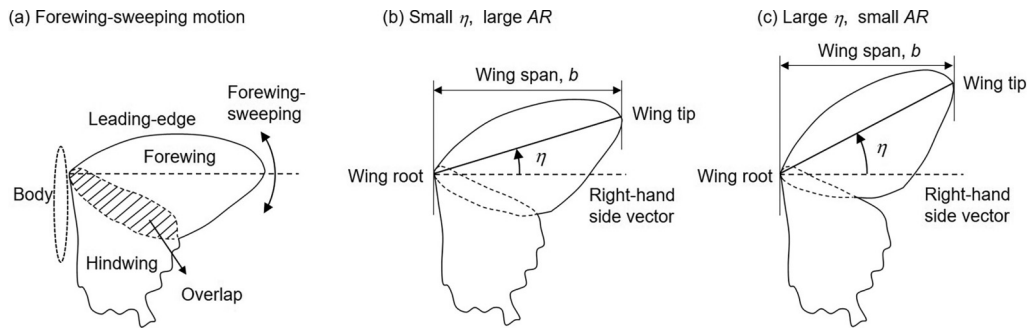[†]Corresponding author: jtyang@ntu.edu.tw

FIG. 1. Schematic of forewing-sweeping motion and definition of wing-swept angle (η).

Chang *et al.* [16] stated that the forewing of *Idea leuconoe* sweeps in both downstroke and upstroke, whereas Ozawa *et al.* [13] showed that the forewing of *P. xuthus* sweeps mainly in a downstroke. We consider the above inconsistency is because of inconsistent aerodynamic effects due to the coupled effects of the wing-swept angle and AR. Because butterfly species have varied forewing and hindwing geometries, when these butterflies perform the same forewing-sweeping motion to change the same wing-swept angle, the changes of AR among these butterflies differ, causing inconsistent aerodynamics effects. To understand how a butterfly utilizes the forewing-sweeping motion to fly, it is essential to decouple the effects of the wing-swept angle and AR and clarify their decoupled effects on flight.

Regarding the effect of the AR, there are abundant studies on it in insect flight, but the results are not entirely consistent. Ansari *et al.* [17], who analyzed flapping wings with several shapes including rectangle, ellipse, and triangle, indicated that, when AR = $2.5 - 15$, the lift force increased with increasing AR, except for the triangular wing. Shahzad *et al.* [18], who analyzed a flapping wing with its shape created by a beta distribution, indicated that, when AR = $1.5 - 6$, the lift coefficient increased with increasing AR. In contrast, Han *et al.* [19], who used inverse Zimmerman wing planforms, found that, during the translation phase of flapping, the lift coefficient increased with AR $\leqslant 3$, and beyond AR = 3, the lift coefficient decreased. Phillips *et al.* [20] analyzed a rectangular flapping wing and showed that the lift coefficient increased with AR $\leqslant 6$, and beyond AR = 6, the lift coefficient decreased. As the aerodynamic forces during the translation phase of the flapping wing are like those in the revolving wing [21], some researchers used revolving wings for study. Kruyt *et al.* [22] analyzed rectangular revolving wings with AR = $2 - 10$ and indicated that, in a small angle of attack ($< 20°$), the lift coefficient increased with increasing AR. Lee *et al.* [23], who considered the Rossby number (Ro), another parameter to describe wing shape, reported that, for rectangular revolving wings with AR = $1 - 10$, under fixed Ro, the lift coefficient increased with AR. In contrast, Luo and Sun [24] created revolving-wing models based on the real wing shape of insects and found that the lift coefficient varied little in AR = $2.8 - 5.5$. Carr *et al.* [25] and Garmann and Visbal [26] used rectangular revolving wings and respectively indicated that the lift coefficients changed little in AR = $1 - 4$. Because the flight of an insect is affected by various parameters including AR, Ro, Reynolds number (Re), and wing kinematics,

when one tunes the wing dimension to change AR for study, the other parameters may change, making the result not purely caused by AR; this may be a reason for the inconsistent results among the above studies. Interestingly, Harbig *et al.* [27] and Bhat *et al.* [14,28] found that using the wing span rather than the wing chord to scale Re and Ro is more appropriate to separate the effect of AR from the effects of Re and Ro. Bhat *et al.* [14,28] indicated that, with the span-based Re and Ro, the force results of the preceding studies became consistent; these authors showed also that, for a revolving wing under span-based Re = $300 - 4000$ with no wing-root offset from the rotational axis, the maximum lift coefficient occurs for AR = $3 - 5$, which is in accordance with most insects [14]. The studies of Harbig *et al.* [27] and Bhat *et al.* [14,28] not only show the importance of the decoupling but also provide a possible way to finding a general wing configuration in insect flight. However, unlike most other insects, the AR of butterflies is small, typically between 1 and 2.5 [3], which is different from the AR range for the maximum lift coefficient reported by Bhat *et al.* [14]. Also, butterflies generate positive lift in downstrokes and negative lift in upstrokes [7]; this characteristic is not captured in the revolving-wing model. The decoupled effect of AR on butterfly flight needs further investigation.

As for the effect of the wing-swept angle, it is found that the wing-swept angle of a butterfly alters a pitching moment via the change of the center of pressure [29,30]. As the wing-swept angle affects the orientation of the leading edge (Fig. 1), this angle might also exert a dominant factor on the formation of a leading-edge vortex (LEV), which is regarded as the primary mechanism for insects to generate lift [31–35]. The effect of the wing-swept angle on lift generation in butterfly flight is, however, rarely discussed. Ancel *et al.* [36] created wing-shape models with varied forewing-sweeping orientations based on the real wings of four butterfly species; these authors indicated that, in a small angle of attack ($\sim 8°$), when the forewing swept backward, the LEV became larger, leading to greater lift and drag; they also showed that the maximum lift-to-drag ratio occurred at zero wing-swept angle which maximized AR. Nevertheless, the wing-swept angle, AR, and span-based Re simultaneously changed in their model; whether the behaviors of the LEV and aerodynamic forces were due to an effect of the wing-swept angle, AR, or span-based Re was unclear. This situation resembles the decoupling issue encountered in the studies of AR. As pointed out above, the flight of an insect contains multiple
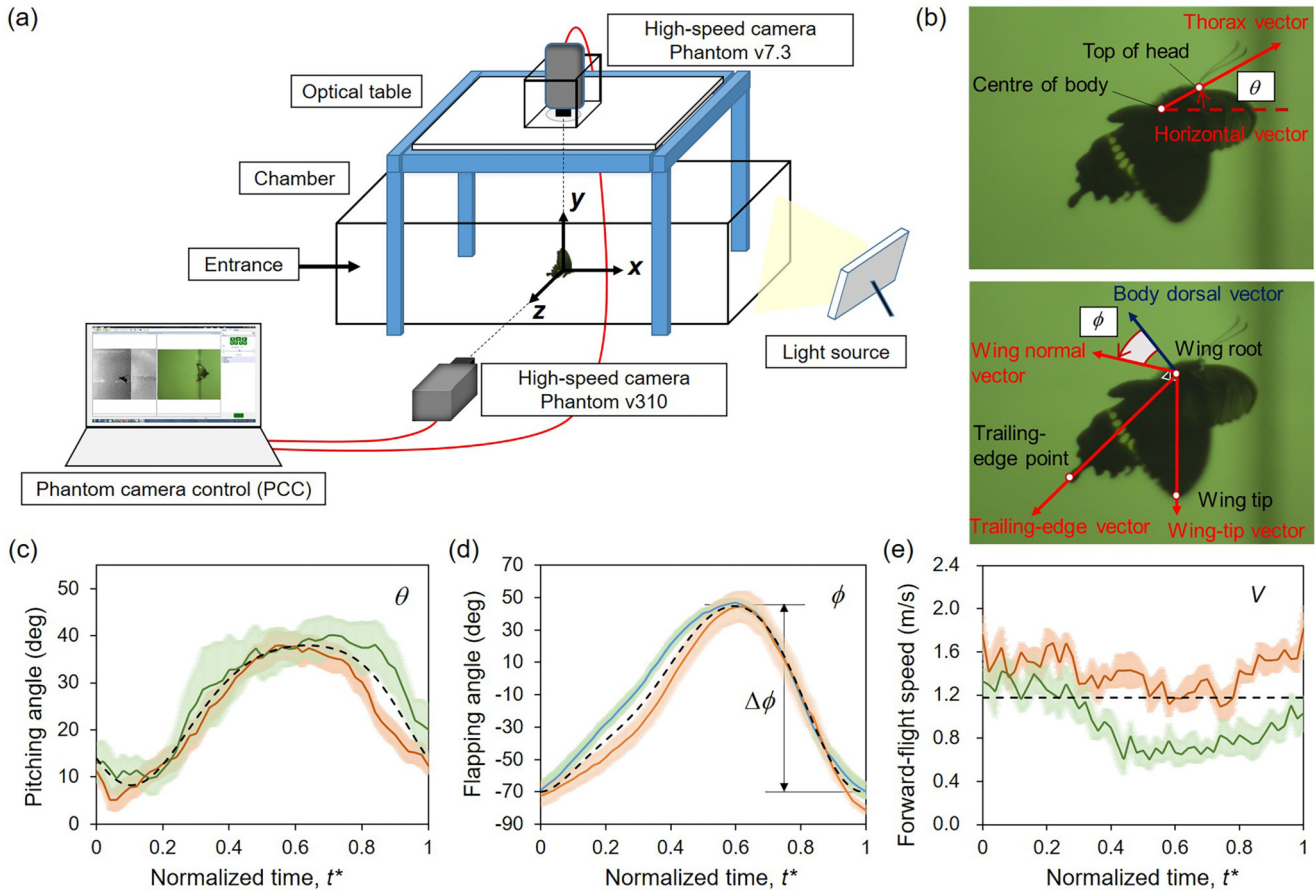
FIG. 2. (a) Schematic of the experiment. (b) Definition of body-pitching and wing-flapping angles. Experimental data of (c) body-pitching angle, (d) wing-flapping angle, and (e) forward-flight speed. In (c)–(e), the solid lines and colored areas represent the average and standard error of the mean (SEM) of *Papilio polytes* (colored red) and *Kallima inachus* (colored green), respectively; the dashed lines are the total average between the two butterfly species used in the simulation.

effects including the wing-swept angle, AR, Re, and wing kinematics effects; decoupling one effect from the others is difficult. An appropriate method of decoupling the effects of the wing-swept angle and AR from the other effects in butterfly flight is lacking. If we seek to apply a flight control method of forewing-sweeping motion to the wing design of a MAV, it is essential to develop a decoupling method of the wing-swept angle and AR and clarify which factor makes the aerodynamic force and flow field alter when the forewing sweeps.

The objective of this paper is to clarify the decoupled effects of the wing-swept angle and AR on a forward-flying butterfly. To decouple the effects of wing-swept angle and AR, we constructed a dimensionless method and a series of wing-shape models with varied combinations of wing-swept angle and AR based on the experimental measurement of two butterfly species (*P. polytes* and *Kallima inachus*). As the analyzed flying mode was a flapping forward flight, we introduced an advance ratio (J); to eliminate other effects, inspired by Harbig *et al.* [27] and Bhat *et al.* [14,28], we adopted a span-based Re and fixed it (Re = 3400) and the advance ratio ($J = 0.65$) and employed the same wing and body motions in the models. We then conducted numerical simulations to analyze the individual flow mechanisms caused by the wing-swept angle and AR and combined them to

analyze their coupled effect (forewing-sweeping motion) on flight.

This paper is organized as follows. In Sec. II, we describe the experimental measurement, decoupling method, and numerical model. In Sec. III A, we indicate the decoupled effects of the wing-swept angle and AR. In Secs. III B and III C, we analyze separately the flow mechanisms caused by the wing-swept angle and AR; in Sec. III D, we combine their effects and analyze their coupled effect on flight. We conclude in Sec. IV.

II. MATERIALS AND METHODOLOGY

A. Experiment and numerical model

The research butterfly species were *P. polytes* and *K. inachus*; they were subscribed from Mu Sheng Insect Museum in Nantou, Taiwan.

To create the numerical models, we first measured the flight kinematics of *P. polytes* and *K. inachus* [Fig. 2(a)]. This experimental method has been applied to various insect species in our previous research (dragonflies [37], damselflies [38,39], and butterflies [8,9,16,40]). In the experiment, we used two high-speed cameras (Phantom v7.3 and Phantom v310) aligned orthogonally to photograph a butterfly flying freely in a chamber ($350 \times 350 \times 1000\,\mathrm{mm}^3$). Both cameras
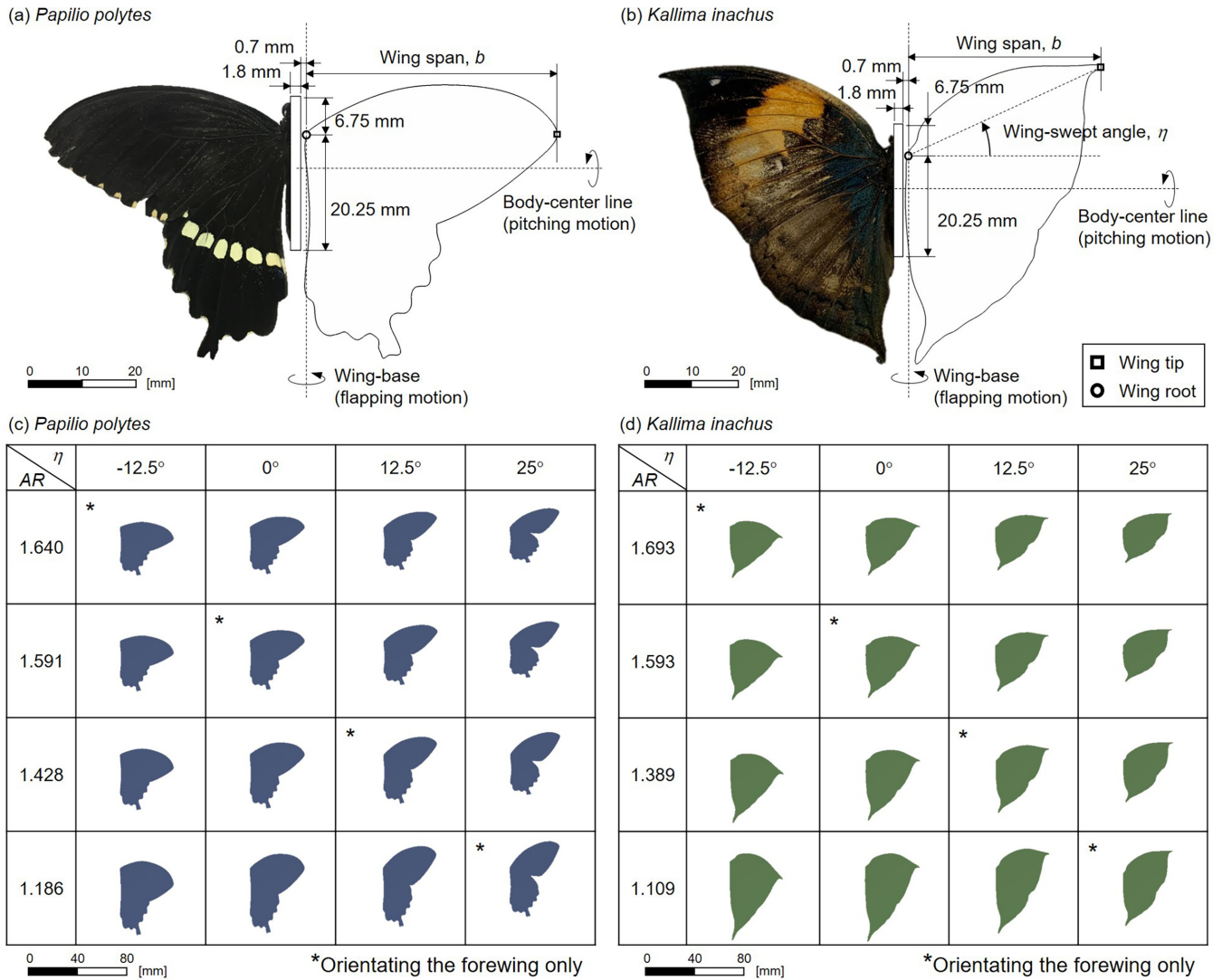
FIG. 3. Top view of experimental butterflies and wing models in (a) and (c) *Papilio polytes* and (b) and (d) *Kallima inachus*.

were operated at 1000 frames per second with resolution 1024×1024. With the photographed films, we applied software (Image J) to mark five characteristic points on a butterfly; these five points were a wing root, a wingtip, a wing trailing-edge point, the center of the body, and the top of the head [Fig. 2(b)]. Each camera recorded two coordinates of the marked points; with two cameras, the three complete coordinates and the corresponding flying motion were obtained. Forward-flight speed V was measured with the horizontal coordinate of the center of the body relative to the ground. Body-pitching angle θ was measured with the angle between the thorax vector and the horizontal vector. Wing-flapping angle ϕ was measured with the wing-normal vector and the body-dorsal vector, in which the wing-normal vector is orthogonal to the wingtip vector and the wing trailing-edge vector [Fig. 2(b)]. On counting the number of frames, the wing-flapping period was obtained. Figures 2(c)–2(e) show the results of the experiment. The butterfly samples numbered six for each species ($N = 6$ for *P. polytes* and $N = 6$ for *K. inachus*). The normalized time t^* was defined as the real time divided by the wing-flapping period. Further detailed de-

scription of the experimental method appears in our preceding articles [16,38,40].

For the establishment of the varied wing shapes in the models, we used software (SolidWorks) to depict the shape of the wings via the experimental photographs (Fig. 3). The forewing and hindwing in each model overlapped partially and were assumed as a single surface with a thickness of 0.4 mm. To create wings with varied wing-swept angles and ARs, we oriented the forewing with a wing-swept angle by $\eta = -12.5°$, $0°$, $12.5°$, and $25°$; this wing set is ordered in diagonal lines from upper left to lower right in Figs. 3(c) and 3(d). The real wing shape in the experimental photographs of *P. polytes* corresponds to $\eta = 0°$ and AR = 1.591; that of *K. inachus* corresponds to $\eta = 25°$ and AR = 1.109. As orienting the forewing simultaneously altered the AR of the entire wing, to analyze the decoupled effects of the wing-swept angle and AR, we then elongated or shortened the wings in a chordwise direction to keep the AR constant compared with each row. In Figs. 3(c) and 3(d), each row represents the wings with varied wing-swept angles and with a fixed AR; each column represents the wings with varied ARs and with
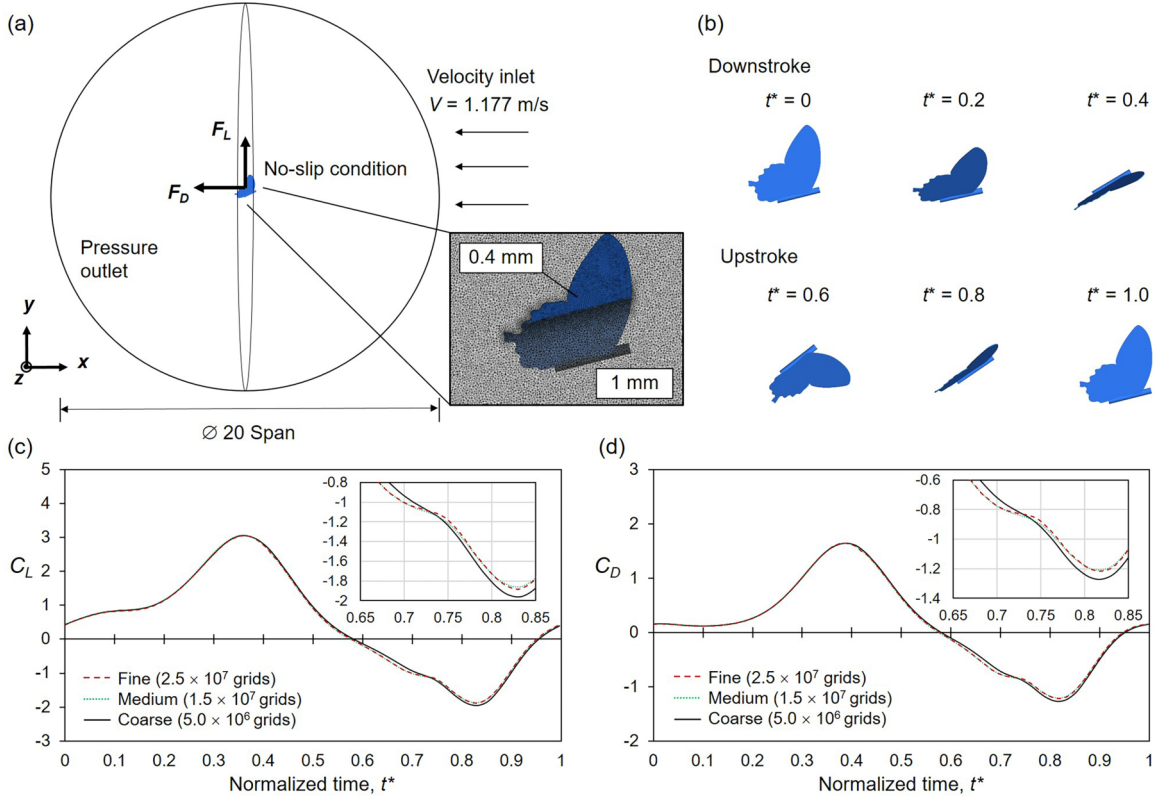
FIG. 4. (a) Flow domain and boundary conditions. (b) Motion of the butterfly model. (c) and (d) Test of grid independence with $\eta = 12.5°$ and AR $= 1.428$.

a fixed wing-swept angle. On comparing the aerodynamic performance in each row and each column, the effects of the wing-swept angle and AR are decoupled and can hence be analyzed individually. According to the research [41,42], the vortex interaction between the body and the wing of an insect is little; in the models, we approximated the body as a cylinder (radius = 1.8 mm, length = 27 mm); the wing root was connected at one-quarter body length from the head with gap distance 0.7 mm. As the models had varied wing-swept angles and ARs, the wing flexibility caused the wings to deform in unequal levels across the models; to analyze the pure effects of the wing-swept angle and AR, we assumed the wings in the models to be rigid and not to twist during flapping. We noted that, in each model, the wing-swept angle and AR were fixed, which did not vary with time during simulation; however, for a real butterfly, the wing-swept angle is reported to change with time during flying [11–13,16]. Because AR varies with the wing-swept angle (Fig. 1), to decouple the effects of the wing-swept angle and AR, it is necessary to separately fix the wing-swept angle and AR. In this paper, we hence fixed the wing-swept angle and AR in each model and separately varied them across the models [Figs. 3(c) and 3(d)].

B. Dimensionless method and parameter setups

In the simulation, the butterfly was fixed at an origin, experienced a constant airflow velocity (forward-flight speed), and simultaneously pitched its body and flapped its wings [Figs. 4(a) and 4(b)]. The global coordinates *xyz* are defined as an inertial ground frame with the axes respectively represent-

ing the front, upper, and right sides. The body pitches about the center of the body; the wings flap about the wing-base axis, a line parallel to the body through the wing root and pitching together with the body [Figs. 3(a) and 3(b)]. The definition of the body-pitching angle and the wing-flapping angle are the same as those used in the experiment [Fig. 2(b)].

The parameters that affect aerodynamic force in the simulation are the body-pitching motion (θ), wing-flapping motion (ϕ), wing-swept angle (η), wingspan (b), mean chord ($\bar{c}$), flapping frequency (f), forward-flight speed (V), air density (ρ), air viscosity (μ), and time (t). The dimensionless parameters that affect lift (C_L) and drag coefficients (C_D) are

$$\frac{F_L}{\frac{1}{2}\rho(2fb\Delta\phi)^2b\bar{c}} = g\left(\eta, \frac{b}{\bar{c}}, \frac{\rho Vb}{\mu}, \frac{V}{2fb\Delta\phi}, \theta, \phi, ft\right), \quad (1)$$

$$\frac{F_D}{\frac{1}{2}\rho(2fb\Delta\phi)^2b\bar{c}} = g\left(\eta, \frac{b}{\bar{c}}, \frac{\rho Vb}{\mu}, \frac{V}{2fb\Delta\phi}, \theta, \phi, ft\right), \quad (2)$$

$$C_L \equiv \frac{F_L}{\frac{1}{2}\rho(2fb\Delta\phi)^2b\bar{c}}, \quad (3)$$

$$C_D \equiv \frac{F_D}{\frac{1}{2}\rho(2fb\Delta\phi)^2b\bar{c}}, \quad (4)$$

$$\text{AR} \equiv \frac{b}{\bar{c}}, \quad (5)$$

$$\text{Re} \equiv \frac{\rho Vb}{\mu}, \quad (6)$$

$$J \equiv \frac{V}{2fb\Delta\phi}, \quad (7)$$

$$t^* \equiv ft, \quad (8)$$

in which F_L is the lift force normal to the ground, and F_D is the drag force parallel to the ground [Fig. 4(a)]. Here, $b\bar{c}$ is the wing surface area, $2fb\Delta\phi$ is the mean wingtip speed during a flapping cycle, and $\Delta\phi$ is the total flapping amplitude [Fig. 2(d)].

To decouple the effects of the wing-swept angle and AR, from Eqs. (1) and (2), the remaining dimensionless parameters θ, ϕ, Re, and J must be fixed when varying η or AR. The body-pitching motion (θ) and wing-flapping motion (ϕ) used in the simulation were adopted as the average motions of the two butterfly species [Eqs. (9) and (10)]:

$$\theta(t) = 25.871° - 10.945°\cos(2\pi ft) - 0.953°\cos(4\pi ft)$$
$$- 0.113°\cos(6\pi ft) - 9.875°\sin(2\pi ft)$$
$$- 2.661°\sin(4\pi ft) - 0.266°\sin(6\pi ft), \qquad (9)$$

$$\phi(t) = -12.645° - 51.264°\cos(2\pi ft) - 4.794°\cos(4\pi ft)$$
$$- 1.177°\cos(6\pi ft) - 19.137°\sin(2\pi ft)$$
$$+ 8.619°\sin(4\pi ft) + 1.743°\sin(6\pi ft), \qquad (10)$$

for which these average motions were obtained with discrete Fourier transformation from the total average of the experimental data [dashed lines in Figs. 2(c) and 2(d)]. The forward-flight speed used in the simulation was set as $V = 1.177$ m s^{-1}, the same as the average forward-flight speed measured in the experiment [dashed line in Fig. 2(e)]. The average Reynolds numbers measured in the experiment were 4278 for *P. polytes* and 2579 for *K. inachus*; in the simulation, we set Re = 3400. The average advance ratios measured in the experiment were 0.85 for *P. polytes* and 0.49 for *K. inachus*; in the simulation, we set $J = 0.65$. In Eqs. (6) and (7), the Reynolds number and the advance ratio include the wingspan b, which varies with the wing shape. To maintain the Reynolds number and the advance ratio fixed across the models, we adjusted the flapping frequency (f) and the air viscosity (μ). Similar methods of adjusting viscosity to maintain Re were adopted in previous research [14,27]. The complete parameter setups that we used in the simulation are listed in Tables I and II.

We noted that, referring to research in which the authors indicated that using a wing span to scale Re is more appropriate to decouple the effect of AR from Re [14,27,28], the Reynolds number in this paper was defined based on the wing span [Eq. (6)]. In addition, according to our previous research [8], the flight speed of a real butterfly is transient, which means Re and J vary with time. However, the purpose of this paper is to clarify the decoupled effects of the wing-swept angle and AR; to eliminate the effects of transient Re and J, it is necessary to fix the flight speed. In this paper, we hence adopted a constant forward-flight speed ($V = 1.177$ m s^{-1}) for analysis. From Eqs. (3) and (4), the mean wingtip speed ($2fb\Delta\phi$) was chosen to scale the force coefficients. As J was constant and the Rossby number (Ro) varied little across the models (Table I), choosing the mean wingtip speed ($2fb\Delta\phi$), forward-flight speed ($2fb\Delta\phi J$), or mean speed of the radius of gyration ($2fb\Delta\phi$Ro) to scale force coefficients did not alter the conclusion of this paper.

C. Numerical scheme and the independence test of grids

We employed commercial software (ANSYS FLUENT 2020R1) with a finite-volume method to solve the flow field of the forward-flying butterfly [Fig. 4(a)]. The flow domain was a sphere of diameter 20 times a wingspan ($\sim$900 mm), chosen to prevent the outlet from interfering with the flow field near the butterfly. The front external surface was a velocity inlet; the rear external surface was a pressure outlet (gauge pressure $= -\rho gy$). On the surface of the butterfly, a no-slip condition was adopted. The average Reynolds number measured in the experiment was $\sim$3400 (Sec. II B); we assumed the flow to be incompressible and laminar and neglected heat transfer. The governing equations of the flow field are

$$\nabla \cdot \mathbf{u} = 0, \qquad (11)$$

$$\rho\left(\frac{\partial\mathbf{u}}{\partial t} + \mathbf{u}\cdot\nabla\mathbf{u}\right) = -\nabla P + \mu\nabla^2\mathbf{u} + \rho\mathbf{g}, \qquad (12)$$

in which $\mathbf{u}$ is the flow velocity field, P is the gauge pressure field, and $\mathbf{g}$ is gravity acceleration ($g = 9.81$ m s^{-2}). The values of air density (ρ) and viscosity (μ) corresponding to various wing-shape models are listed in Table II.

To mesh the numerical grids, the grid topology was a tetrahedron. Near the butterfly, the grid size was set as 1 mm; on the wing surface, the grid size was set as 0.4 mm. For the pressure-velocity coupling, the semi-implicit method for pressure-linked equations-consistent (SIMPLEC) was applied. For the spatial discretization, the Green-Gauss node-based and second-order upwind methods were applied. Smoothing and local-remeshing methods were adopted for the dynamic mesh strategy. The total grid number was $\sim$2.5$\times$10^7. In each flapping period, the time steps numbered 400; the time step size (Δt) corresponding to various models is listed in Table II.

The credibility of the above numerical scheme has been verified for various insect species in our previous research (dragonflies [37], damselflies [38,39], and butterflies [8,9,16,40]). In this paper, we additionally used three grid numbers: coarse (5$\times$10^6 grids), medium (1.5$\times$10^7 grids), and fine (2.5$\times$10^7 grids) cases to validate the independence of the grids. Figures 4(c) and 4(d) show the results of the independence test. The values of the lift and drag in the medium and fine cases were similar, whereas those in the coarse case deviated. The mean lift and drag over a flapping cycle in the fine case varied $\sim$0.312% and 0.499%, respectively, compared with those in the medium case. These conditions indicate that the result in the fine case has become nearly convergent, showing the effectiveness of the grid-number setup. In the following sections, we hence adopted 2.5$\times$10^7 grids for the simulation.

III. RESULTS AND DISCUSSION

A. Decoupled effects of wing-swept angle and AR on aerodynamic forces

In nature, a butterfly flies with a forewing-sweeping motion relative to a hindwing [11–13], which alters not only the wing-swept angle but also the AR of the entire wing (Fig. 1); the effects of the wing-swept angle and AR on aerodynamics

TABLE I. Information of wing models.

Wing-swept angle, η (deg)	AR	Wingspan, b (mm)	Mean chord, $\bar{c}$ (mm)	Wing area, $b\bar{c}$ (mm^2)	Radius of gyration, r_g (mm)	Ro[a]
Papilio polytes						
	1.640	43.322	26.420	1144.572	20.164	0.465
−12.5	1.591	43.322	27.238	1180.024	20.172	0.466
	1.428	43.322	30.351	1314.855	20.170	0.466
	1.186	43.322	36.536	1582.806	20.161	0.465
	1.640	44.374	27.062	1200.834	20.467	0.461
0	1.591	44.374	27.892	1237.663	20.461	0.461
	1.428	44.374	31.087	1379.445	20.461	0.461
	1.186	44.374	37.421	1660.536	20.459	0.461
	1.640	43.323	26.416	1144.393	20.076	0.463
12.5	1.591	43.323	27.228	1179.599	20.075	0.463
	1.428	43.323	30.346	1314.648	20.075	0.463
	1.186	43.323	36.538	1582.897	20.075	0.463
	1.640	40.217	24.527	986.407	19.036	0.473
25	1.591	40.217	25.283	1016.825	19.046	0.474
	1.428	40.217	28.183	1133.426	19.045	0.474
	1.186	40.217	33.907	1363.621	19.037	0.473
Kallima inachus						
	1.693	42.895	25.332	1086.604	18.739	0.437
−12.5	1.593	42.895	26.930	1155.158	18.737	0.437
	1.389	42.895	30.893	1325.157	18.735	0.437
	1.109	42.895	38.697	1659.893	18.739	0.437
	1.693	43.935	25.950	1140.127	19.469	0.443
0	1.593	43.935	27.572	1211.377	19.471	0.443
	1.389	43.935	31.624	1389.433	19.470	0.443
	1.109	43.935	39.625	1740.927	19.471	0.443
	1.693	42.893	25.326	1086.291	19.641	0.458
12.5	1.593	42.893	26.933	1155.234	19.642	0.458
	1.389	42.893	30.884	1324.682	19.641	0.458
	1.109	42.893	38.673	1658.793	19.639	0.458
	1.693	39.817	23.522	936.565	19.290	0.484
25	1.593	39.817	24.996	995.269	19.292	0.485
	1.389	39.817	28.679	1141.918	19.291	0.484
	1.109	39.817	35.910	1428.828	19.288	0.484

[a]Referring to research [14,28], the Rossby number was defined as a ratio of the radius of gyration to the wingspan (Ro = r_g/b).

TABLE II. Parameter setups.

| η (deg)[a]	ρ (kg m^{-3})	μ (10^{-5} Pa s)	V (m s^{-1})	f (Hz)	Δt (10^{-4} s)	θ (deg)	ϕ (deg)	$\Delta\phi$ (deg)	Re	J
Papilio polytes										
−12.5	1.225	1.837	1.177	10.435	2.396	Eq. (9)	Eq. (10)	114.746	3400	0.65
0	1.225	1.882	1.177	10.188	2.454	Eq. (9)	Eq. (10)	114.746	3400	0.65
12.5	1.225	1.837	1.177	10.435	2.396	Eq. (9)	Eq. (10)	114.746	3400	0.65
25	1.225	1.705	1.177	11.241	2.224	Eq. (9)	Eq. (10)	114.746	3400	0.65
Kallima inachus										
−12.5	1.225	1.819	1.177	10.539	2.372	Eq. (9)	Eq. (10)	114.746	3400	0.65
0	1.225	1.863	1.177	10.290	2.430	Eq. (9)	Eq. (10)	114.746	3400	0.65
12.5	1.225	1.819	1.177	10.540	2.372	Eq. (9)	Eq. (10)	114.746	3400	0.65
25	1.225	1.688	1.177	11.354	2.202	Eq. (9)	Eq. (10)	114.746	3400	0.65

[a]Information of varied AR wings is included.
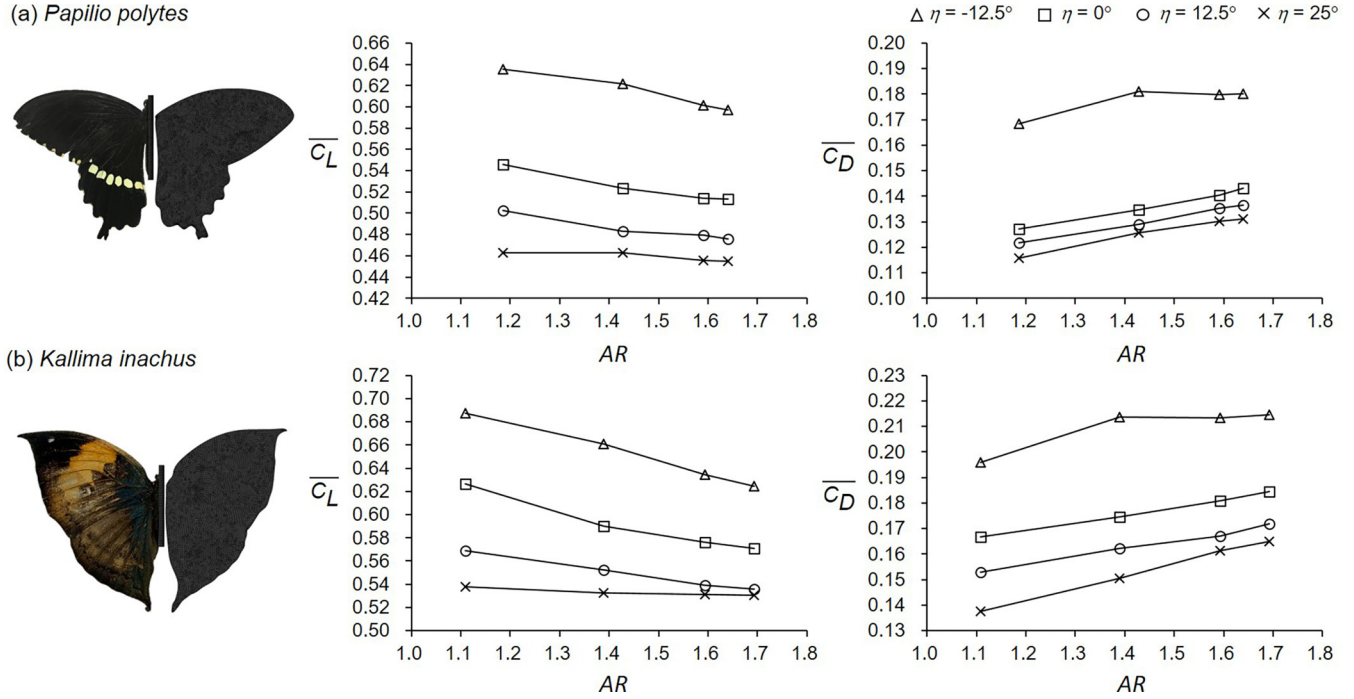
FIG. 5. Mean lift and drag coefficients over a flapping cycle with varied wing-swept angles and aspect ratios in (a) *Papilio polytes* and (b) *Kallima inachus*.

are coupled. In this paper, we created wing-shape models with varied combinations of wing-swept angle and AR and analyzed their effects on flight.

Figure 5 shows the mean lift and drag coefficients over a flapping cycle with varied wing-swept angles and ARs in *P. polytes* and *K. inachus*. The force coefficients in *P. polytes* and *K. inachus* overall show a similar trend. For a fixed AR, as η decreases, the mean lift and drag increase; for a fixed η, as AR decreases, the mean lift increases and the mean drag decreases. Figure 6 presents the instantaneous forces generated in the cycle. Positive lift and drag are generated during a downstroke ($t^* = 0 - 0.6$), and negative lift and drag are generated during an upstroke ($t^* = 0.6 - 1$); this trend is in accordance with previous research [7,16,40,43,44]. For a fixed AR, as η decreases, the lift and drag in the downstroke increase but vary little in the upstroke [Fig. 6(a)]; this condition indicates that the increases of mean lift and drag with decreasing η shown in Fig. 5 are due mainly to the forces generated in the downstroke. In contrast, for a fixed η, as AR decreases, the lift and drag in the downstroke increase, and those in the upstroke decrease [Fig. 6(b)]. At an early stage of upstroke ($t^* = 0.6 - 0.75$), the changes of the forces caused by AR [Fig. 6(b)] are larger than those caused by η [Fig. 6(a)]. Table III lists the normalized lift and drag impulses generated in the downstroke and upstroke in varied AR cases with fixed η. The normalized lift impulse (I_L^*) and drag impulse (I_D^*) are defined as

$$I_L^* = \int C_L dt^* \quad \text{and} \quad I_D^* = \int C_D dt^*, \qquad (13)$$

which are equivalent to the area below the force curves in each half-stroke in Fig. 6(b). In Table III, for a fixed η, as AR decreases, the increased magnitude of lift impulse in

the downstroke is larger than the decreased magnitude of lift impulse in the upstroke, and the increased magnitude of drag impulse in the downstroke is smaller than the decreased magnitude of drag impulse in the upstroke. Over a flapping cycle, the mean lift and drag hence increases and decreases, respectively, with decreasing AR (Fig. 5).

According to the above results, the force trends caused by η and AR are distinct but consistent in the two butterfly species (Fig. 5). The effect of η on the forces remains unchanged in varied AR [Fig. 6(a)], and the effect of AR on the forces remains unchanged in varied η [Fig. 6(b)]. These conditions indicate that, through the wing-shape models and the dimensionless method established in this paper, the effects of η and AR were decoupled. In Secs. III B and III C, we hence analyzed their flow mechanisms, respectively.

B. Individual effect of wing-swept angle on flow field

As the effect of η appears mainly in the downstroke [Fig. 6(a)], we focused the analysis thereon. Figure 7 presents the vortex structure and pressure contour with varied η and fixed AR at a middownstroke ($t^* = 0.35$). During the downstroke, the wing flaps forward and downward; vortices roll up from the wing, resulting in a low-pressure region on the top surface of the wing. In each case, a LEV, a wingtip (WTV), and a trailing-edge (TEV) vortex form. Near a wingtip, the outboard LEV and the WTV merge, constructing a compound vortex structure called LEV-WTV. This LEV-WTV then detaches from the wing, dragging a LEV-WTV locus in its wake. On comparing the vortex structure, for both butterfly species and ARs, the sizes of LEV and WTV in the cases $\eta = -12.5°$ are the largest, which produce the longest LEV-WTV loci in its wake (see side and front views in Fig. 7).
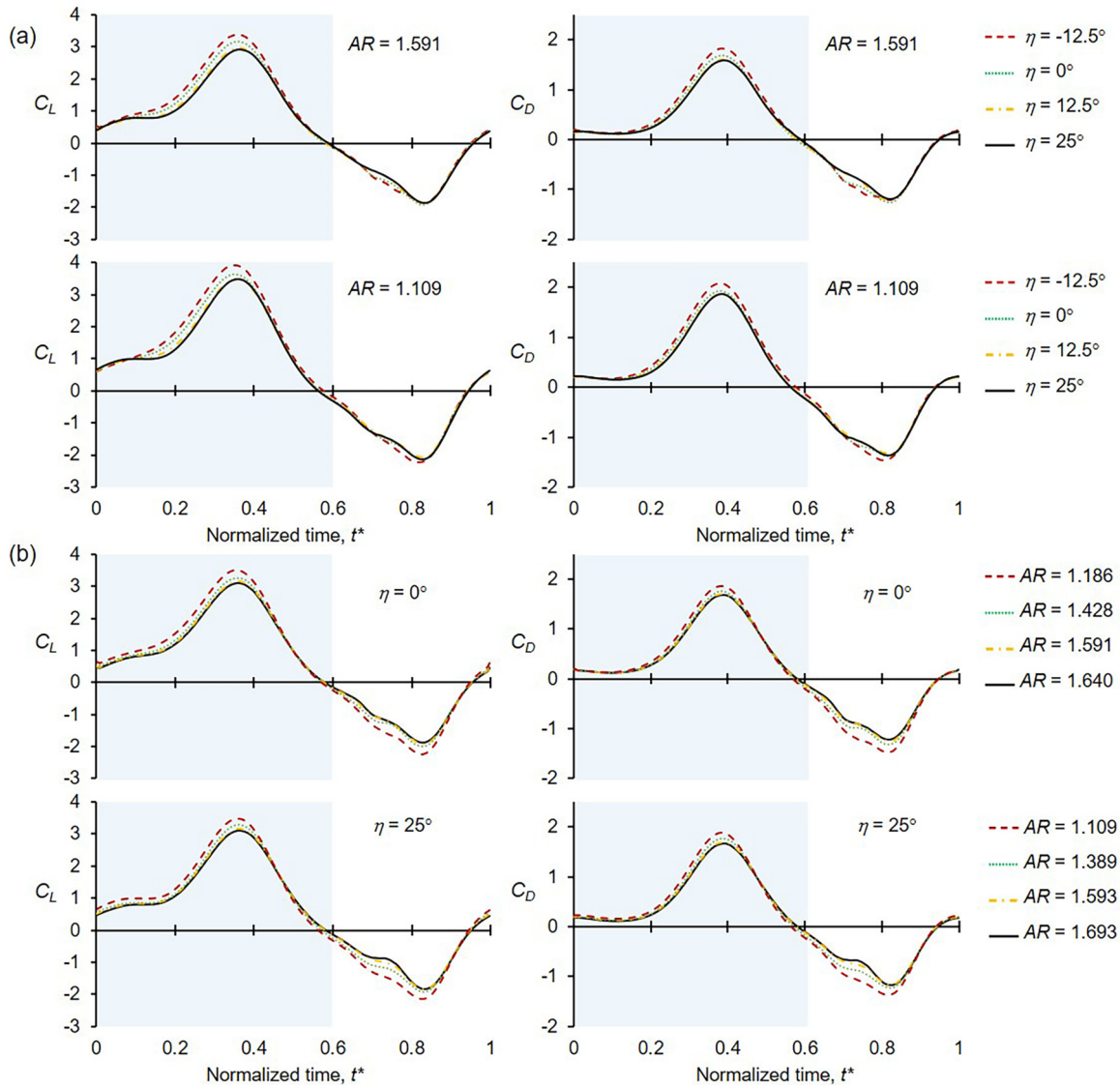
FIG. 6. Lift and drag coefficients in (a) varied wing-swept angles and fixed aspect ratios (ARs) and (b) varied ARs and fixed wing-swept angles.

Regarding the pressure distribution on the wing, Fig. 7 shows that, for both ARs, the case $\eta = -12.5°$ has the largest area of low-pressure region beneath the LEV on the top wing surface. As a region of low pressure represents a position to which a vortex attaches, the LEV in the case $\eta = -12.5°$ is indicated to attach best to the wing. According to the research [31–35], the LEV attachment is affected by three factors: WTV, spanwise flow, and rotational accelerations (centripetal and Coriolis forces). Because in this paper the Rossby number varied little ($\Delta \text{Ro} = 0.01 - 0.05$; Table I) and the wing motions were the same across the models [Eqs. (9) and (10)], the discrepancy of the LEV attachment among varied η cases

TABLE III. Normalized force impulse with varied ARs at fixed wing-swept angles.

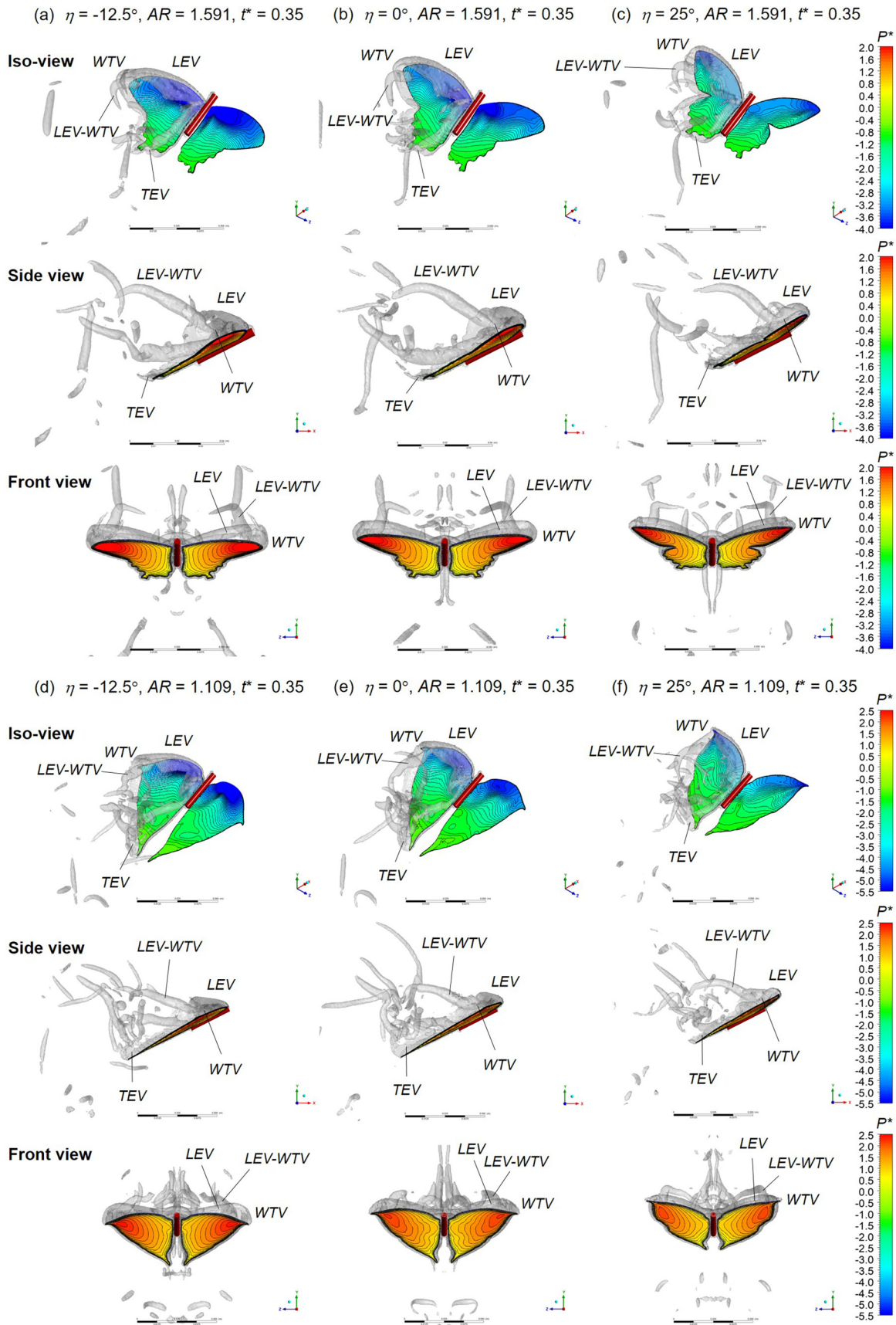|	$\eta = 0°$					$\eta = 25°$			
	Downstroke		Upstroke			Downstroke		Upstroke	
AR	I_L^*	I_D^*	I_L^*	I_D^*	AR	I_L^*	I_D^*	I_L^*	I_D^*
1.186	0.987	0.426	−0.441	−0.299	1.109	0.956	0.417	−0.419	−0.279
1.428	0.908	0.397	−0.385	−0.262	1.389	0.897	0.396	−0.365	−0.246
1.591	0.877	0.386	−0.362	−0.246	1.593	0.870	0.385	−0.338	−0.224
1.640	0.867	0.383	−0.354	−0.239	1.693	0.856	0.380	−0.325	−0.216

FIG. 7. Vortex structure and pressure contour of (a)–(c) *Papilio polytes* and (d)–(f) *Kallima inachus* with varied wing-swept angles and fixed aspect ratios at a middownstroke ($t^* = 0.35$). The vortex structure is identified with a Q criterion according to $Q = 40(2\Delta\phi f)^2$. The pressure is normalized with $P^* = P/[0.5\rho(2\Delta\phi f b)^2]$.
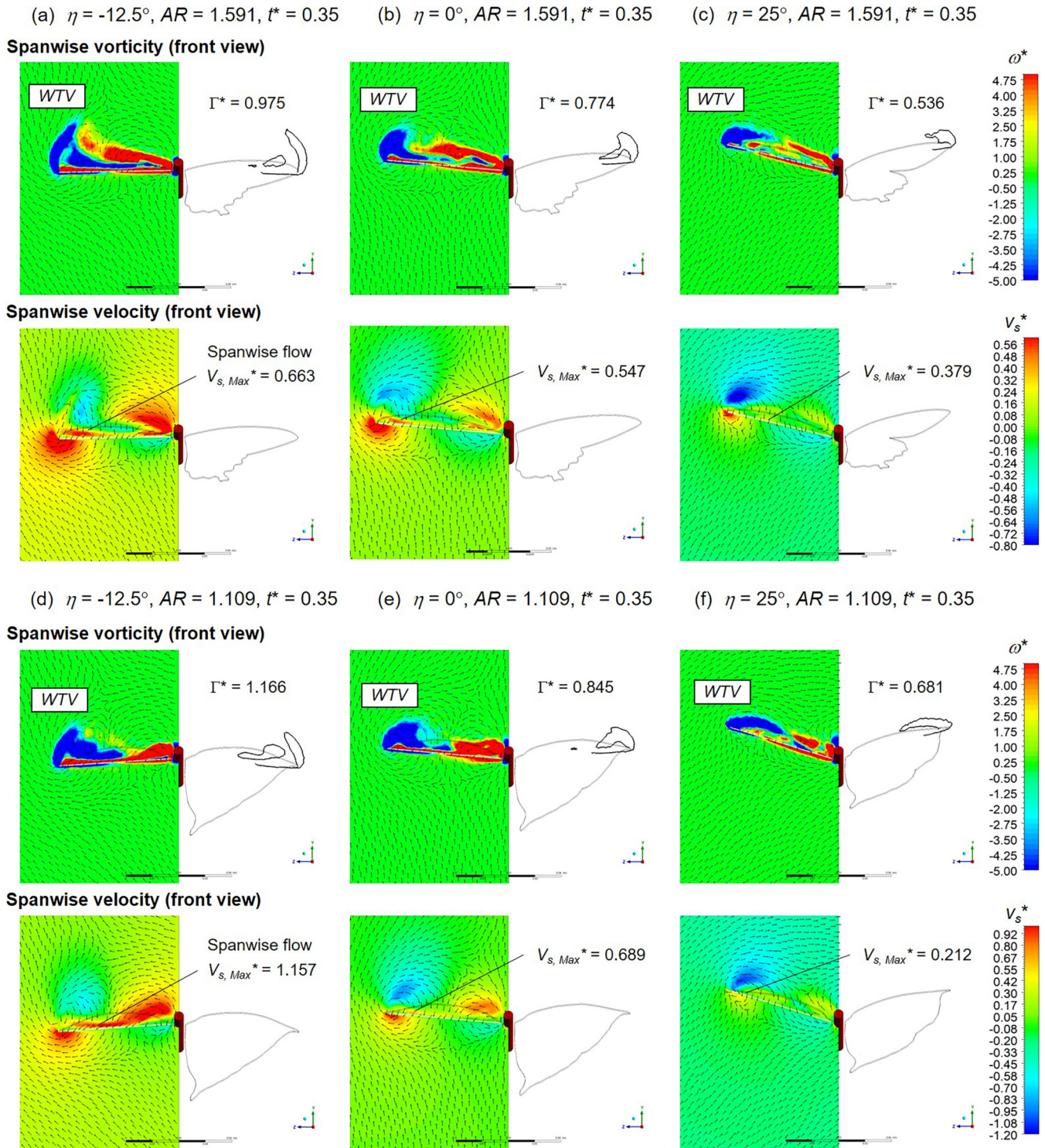
FIG. 8. Spanwise vorticity and velocity contours of (a)–(c) *Papilio polytes* and (d)–(f) *Kallima inachus* with varied wing-swept angles and fixed aspect ratios at a middownstroke ($t^* = 0.35$). The vorticity is normalized with $\omega^* = \omega/(2\Delta\phi f)$. The spanwise velocity is normalized with $V_s^* = V_s/(2\Delta\phi f b)$.

shown in Fig. 7 is due mainly to the WTV and the spanwise flow. Figure 8 displays the vorticity and velocity contours in spanwise planes. A spanwise plane is a plane that lies on the line between a wing root and a wingtip and is orthogonal to the wing surface. The circulation (Γ) induced by a WTV is

quantified with

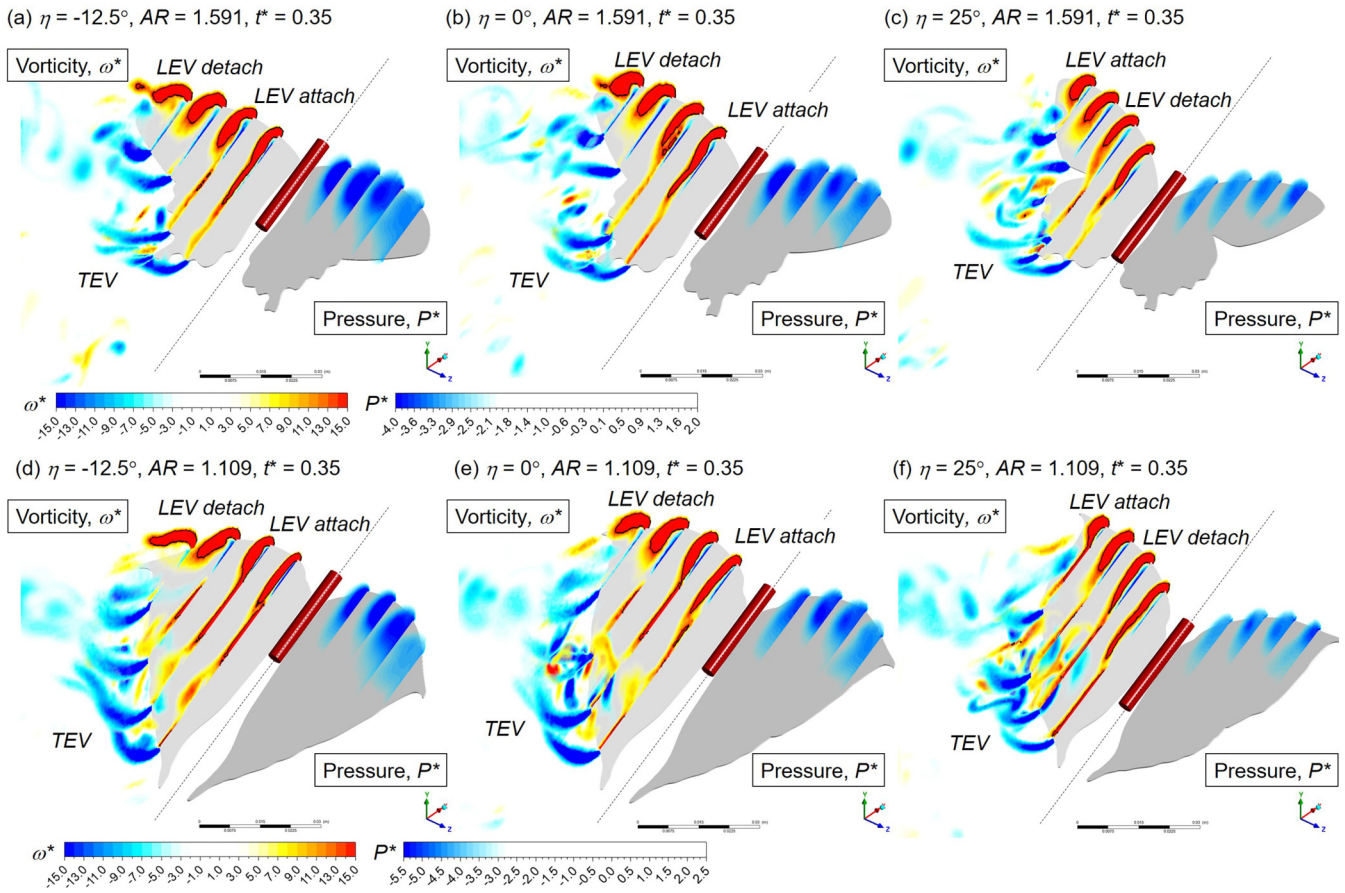$$\Gamma = \iint_S \vec{\omega} \cdot d\vec{S}, \tag{14}$$

FIG. 9. Chordwise vorticity and pressure contours in (a)–(c) *Papilio polytes* and (d)–(f) *Kallima inachus* with varied wing-swept angles and fixed aspect ratios at a middownstroke ($t^* = 0.35$). The vorticity is normalized with $\omega^* = \omega/(2\Delta\phi f)$; the pressure is normalized with $P^* = P/[0.5\rho(2\Delta\phi fb)^2]$. The vorticity contours are depicted at leftwing, and the pressure contours are depicted at rightwing. The black solid lines in the vorticity contours are the contour lines of $\omega^* = 15$.

in which $\vec{\omega}$ is vorticity, and S is an integral area bounded with a vorticity contour line of value $16\Delta\phi f$ (black lines near the wingtips in Fig. 8). The circulation is normalized with $\Gamma^* = \Gamma/(2\Delta\phi fb^2)$. We chose the vorticity contour line of value $16\Delta\phi f$ as the boundary because this value was not too large or too small to display the WTV; we had used other boundary values ($20\Delta\phi f$, $10\Delta\phi f$, and $8\Delta\phi f$) to calculate the circulation, and the trend of the circulations varying with η remained the same among these boundary values. In Fig. 8, for both butterfly species and ARs, the case $\eta = -12.5°$ has the largest vorticity strength of WTV; the corresponding circulations are 0.975 and 1.166 in *P. polytes* and *K. inachus*, respectively, larger than those in the case of $\eta = 25°$. The maximum spanwise flow speed ($V_{S,\max}^*$) in the case $\eta = -12.5°$ are also the largest. The WTV enhances the LEV attachment by providing a downwash flow to decrease the effective angle of attack [32]; the spanwise flow stabilizes the size of LEV by draining the flow momentum from the inboard to the outboard wing [31,34]. From these results, we summarized that a small η wing produces stronger WTV and spanwise flow, which enhances the LEV attaching to the wing. The size of the low-pressure region on the top wing surface therefore increases as η decreases (Fig. 7).

Although in each species the case of $\eta = -12.5°$ has the best LEV attachment that provides the largest low-pressure

region on the top wing surface [Figs. 7(a) and 7(d)], a small low-pressure region emerges on the outboard top wing surface in the case of $\eta = 25°$ [Figs. 7(c) and 7(f)]; this condition indicates that, in the case of $\eta = 25°$, the LEV attaches to the outboard wing. Figure 9 displays the vorticity and pressure contours on the chordwise planes located at 20, 40, 60, and 80% wingspan. In the case $\eta = -12.5°$, the maximum vorticity induced by LEV is near the inboard wing surface but is far from the outboard wing surface; the strength of low pressure along the spanwise direction decreases [Figs. 9(a) and 9(d)]. These conditions indicate that the LEV in the case of $\eta = -12.5°$ attaches to the inboard wing and detaches from the outboard wing. In contrast, in the case of $\eta = 25°$, the maximum vorticity induced by LEV is far from the inboard wing surface but is near the outboard wing surface; the strength of low pressure along the spanwise direction increases [Figs. 9(c) and 9(f)]. These conditions indicate that the LEV in the case of $\eta = 25°$ detaches from the inboard wing and attaches to the outboard wing.

The difference of the location of LEV attachment in varied η cases shown in Fig. 9 is due mainly to a spanwise upstream flow. Figure 10 presents a schematic of spanwise flow. In insect flapping forward flight, the spanwise flow has two sources: (i) wing-flapping motion and (ii) spanwise component of upstream flow caused by a forward-flight speed. The
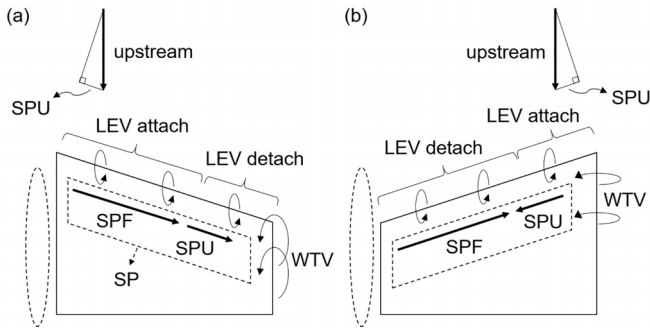
FIG. 10. Schematic of spanwise flow (SP) caused by upstream flow (SPU) and wing-flapping motion (SPF) in (a) backward-swept wing and (b) forward-swept wing.

spanwise flow (SP) comprises the spanwise flow of the wing-flapping motion (SPF) and the spanwise upstream flow (SPU). In Fig. 10(a), for a backward-swept wing, as the SPU is in the same direction as the SPF, these two spanwise flows merge into a strong SP, draining the flow momentum from inboard to outboard wing. When this strong SP flows toward the wingtip, it extrudes the WTV upward and makes the WTV develop better in a wake with an increased strength. These phenomena are observed in Fig. 8, in which in the case $\eta = -12.5°$, the spanwise flow speed is the largest, the shape of WTV is the most stretched upward, and the circulation of WTV is the largest. The LEV in the case $\eta = -12.5°$ hence attaches best to the inboard wing (Fig. 9). In contrast, for a forward-swept wing [Fig. 10(b)], as the SPU is in the opposite direction to the SPF, these two spanwise flows undermine each other, decreasing the spanwise flow near the inboard wing; near the outboard wing, as the SPU flows inward, this inward-flowing SPU presses the WTV toward the wing surface and restricts the development of WTV. In Fig. 8, in the case $\eta = 25°$, the spanwise flow speed near the inboard wing is the least, the WTV is pressed most closely to the wing surface, and the circulation of WTV is the smallest; in addition, near the wingtip, an inward flow appears [blue area in spanwise velocity contours in Figs. 8(c) and 8(f)]. Because in the case $\eta = 25°$, the spanwise flow speed near the inboard wing and the strength of WTV are the least, the LEV detaches from the inboard wing; near the outboard wing, as the inward-flowing SPU drains the flow momentum from the outboard to the inboard wing, the LEV attaches to the outboard wing [Figs. 9(c) and 9(f)].

To summarize, for a backward-swept wing (small η), the upstream flow increases the spanwise flow speed and makes the WTV develop better with an increased strength; the LEV attaches better to the inboard wing and provides a large region of low pressure on the inboard top wing surface [Figs. 7(a) and 7(d)]. In contrast, for a forward-swept wing (large η), although the upstream flow provides an inward flow that makes the LEV attach to the outboard wing, the strength of WTV and the spanwise flow speed near the inboard wing are small; the LEV detaches from the inboard wing, losing most of the region of low pressure on the inboard top wing surface [Figs. 7(c) and 7(f)]. Because the wing flaps forward and downward during the downstroke, the region of low pressure on the top wing surface provides positive lift and drag. The lift and

drag generated in the downstroke, therefore, decreases as η increases [Fig. 6(a)].

C. Individual effect of AR on flow field

As the forewing-sweeping motion simultaneously alters the AR of the wing, in this section, we analyze the individual effect of AR on varying AR and fixing η.

Figure 11 presents the vortex structure, vorticity contour, and pressure contour of *P. polytes* with varied AR and fixed η at middownstroke ($t^* = 0.35$). The vorticity and pressure contours in Fig. 11(a) are depicted on chordwise planes at 20, 40, 60, and 80% wingspan; the pressure contours in Fig. 11(c) are depicted on a chordwise plane at 40% wingspan. As the results of *K. inachus* are like those of *P. polytes*, for the sake of brevity, we present here the cases of *P. polytes*. In Fig. 11(a), the trends of LEV attachment and the pressure distributions along the spanwise direction in the cases AR = 1.640, 1.428, and 1.186 are similar. Near the wing root, the LEV is near the wing surface; near the wingtip, it is far from the wing surface; the strength of low pressure along the spanwise direction decreases. These conditions indicate that the LEV attaches to the inboard wing and detaches from the outboard wing. Nevertheless, at the same wingspan location, the strength of low pressure in the case AR = 1.186 is larger than those in the other two cases [Fig. 11(a)]; this phenomenon is also observed in Fig. 11(b) in which the size of the low-pressure region on the top wing surface in the case AR = 1.186 is the largest. This condition indicates that, at the same wingspan location, the LEV in the case AR = 1.186 attaches best to the wing. The reason is that, to decouple the effect of AR from η under constant Re and J, in this paper, we fixed the wing span and adjusted the wing chord length to create wings with varied AR (Fig. 3); the chord length in the case of AR = 1.186 is greater than those in the cases of AR = 1.640 and 1.428. The wing with AR = 1.186 thus induces a larger area of low-pressure region in its wake due to its greater chord length [Fig. 11(c)]. This larger area of low-pressure region in its wake provides a sufficient suction to make the LEV attach to the wing. The wing of small AR therefore generates larger lift and drag during the downstroke [Fig. 6(b)].

Regarding the effect of AR on an upstroke, Fig. 12 displays the pressure and velocity contours at a wing-reversal stage ($t^* = 0.5 - 0.6$). In this interval, the wing is near the end of the downstroke and prepares to flap backward to begin an upstroke. When the wing performs a downstroke ($t^* = 0 - 0.6$), it induces flow in its wake toward the wing [Figs. 12(a) and 12(c)]; at the beginning of the upstroke ($t^* = 0.6$), the backward-flapping wing captures this induced flow and generates a region of local high pressure on the top surface of the wing [Figs. 12(b) and 12(d)]. This phenomenon is called the wake-capture effect and is regarded as the one of the important mechanisms for insects to generate forces [45–47]. On comparing the cases between AR = 1.186 and 1.640, we found that, because of the greater chord length, the wing of AR = 1.186 induces stronger flow toward the wing [Fig. 12(c)]. At the beginning of the upstroke, this strong induced flow generates a larger area of high-pressure region on the top wing surface [Fig. 12(d)]. This condition indicates that the wake-capture effect is enhanced in the case of small
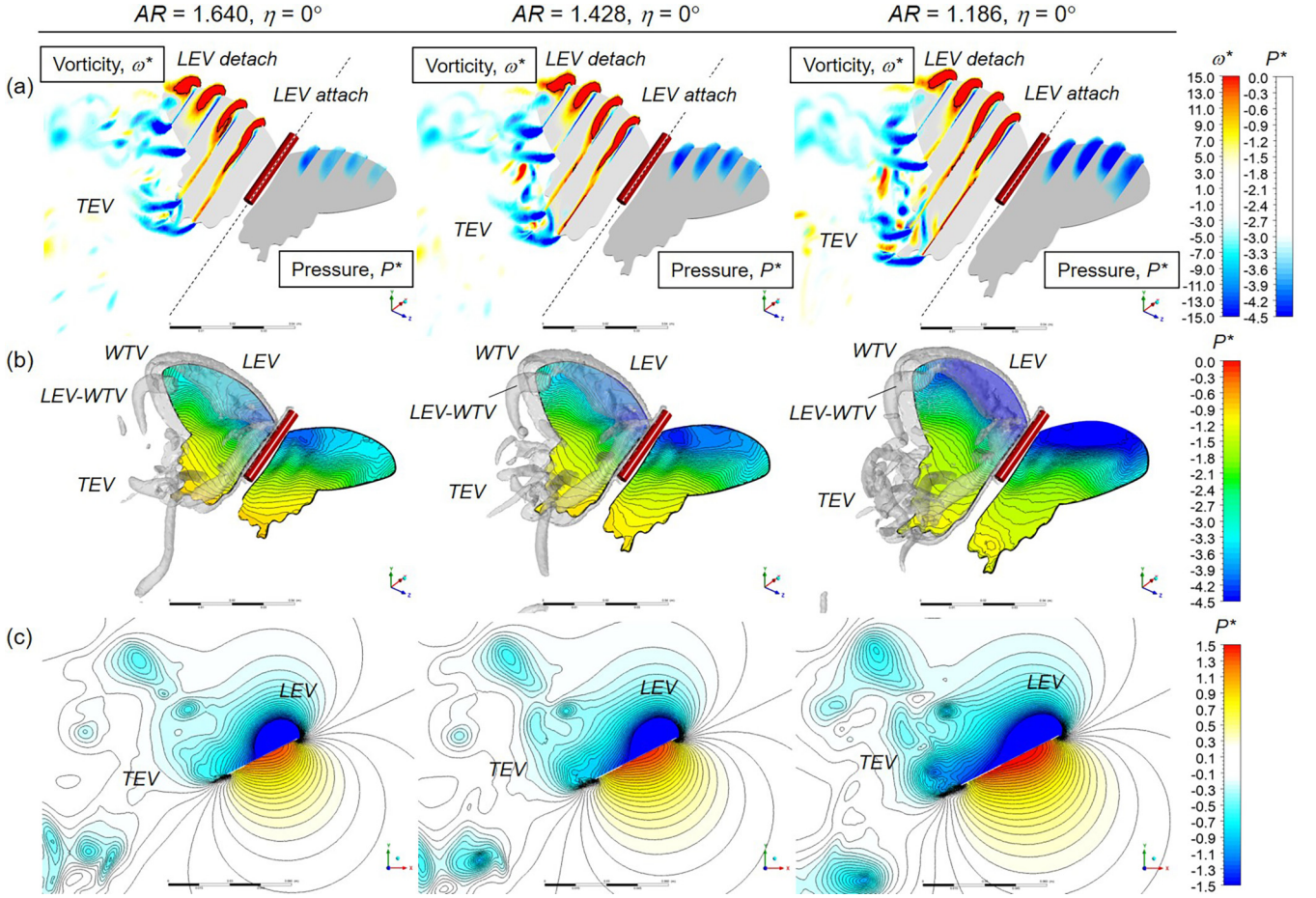
FIG. 11. (a) Vorticity and pressure contours, (b) vortex structure, and (c) pressure contours with varied aspect ratios at a middownstroke ($t^* = 0.35$) in *Papilio polytes*. The pressure is normalized with $P^* = P/[0.5\rho(2\Delta\phi fb)^2]$; the vorticity is normalized with $\omega^* = \omega/(2\Delta\phi f)$. In (a), the vorticity and the pressure contours are depicted at leftwing and rightwing, respectively; the black solid lines in the vorticity contours are the contour lines of $\omega^* = 15$. In (b), the vortex structure is identified with a Q criterion according to $Q = 40(2\Delta\phi f)^2$.

AR. As the body-pitching angle is positive, the high-pressure region on the top wing surface consists of negative values of lift and drag. The enhanced wake-capture effect in the small AR wing explains the significant increases of the negative lift and drag at the early stage of the upstroke [$t^* = 0.6 - 0.75$; Fig. 6(b)].

To confirm that a wing of small AR enhances the wake-capture effect, we isolated the induced flow by conducting a simulation in which the butterfly is initially positioned at the end of the downstroke in still air and impulsively begins an upstroke (denotes ISO simulation). With subtracting the force in the ISO simulation from the force in the original simulation, the force due to the wake-capture effect is quantified:

$$C_{L,\mathrm{WC}} = C_L - C_{L,\mathrm{ISO}} \quad \text{and} \quad C_{D,\mathrm{WC}} = C_D - C_{D,\mathrm{ISO}}. \quad (15)$$

In Eq. (15), subscript ISO denotes the force generated in the ISO simulation, and subscript WC denotes the force caused by the wake-capture effect. The result is shown in Fig. 13. Compared with the ISO simulation, the negative values of lift and drag in the original cases of AR = 1.640 and 1.186 increase at the early stage of the upstroke [$t^* = 0.6 - 0.75$; Figs. 13(a) and 13(b)], which indicates that the wake-capture effect appears in the original cases. In ad-

dition, both the negative values of lift and drag caused by the wake-capture effect ($C_{L,\mathrm{WC}}$ and $C_{D,\mathrm{WC}}$) in the case of AR = 1.186 are larger than those in the case of AR = 1.640 [Fig. 13(c)]. This condition proves that the wake-capture effect is enhanced in the case of a small AR.

D. Coupled effect of wing-swept angle and AR

In previous sections, we analyzed the decoupled effects of η and AR by sequentially fixing AR and η. Nevertheless, for a real butterfly, the effects of η and AR are coupled; as the forewing sweeps forward, η increases and the AR of the entire wing decreases, and vice versa (Fig. 1). In this section, we combined their effects and analyzed their coupled effect on flight.

Figures 14(a) and 14(b) present the mean lift and drag over a flapping cycle with the real data of the wing-swept angle and AR of *P. polytes* and *K. inachus*. The real data were obtained on orienting the forewing in the photographs of the experimental butterflies and are listed in diagonal lines from upper left to lower right in Figs. 3(c) and 3(d). Overall, the mean forces in *P. polytes* and *K. inachus* have a similar trend. As η increases and the corresponding AR decreases, the mean lift and drag decrease. Figures 14(c) and 14(d) show
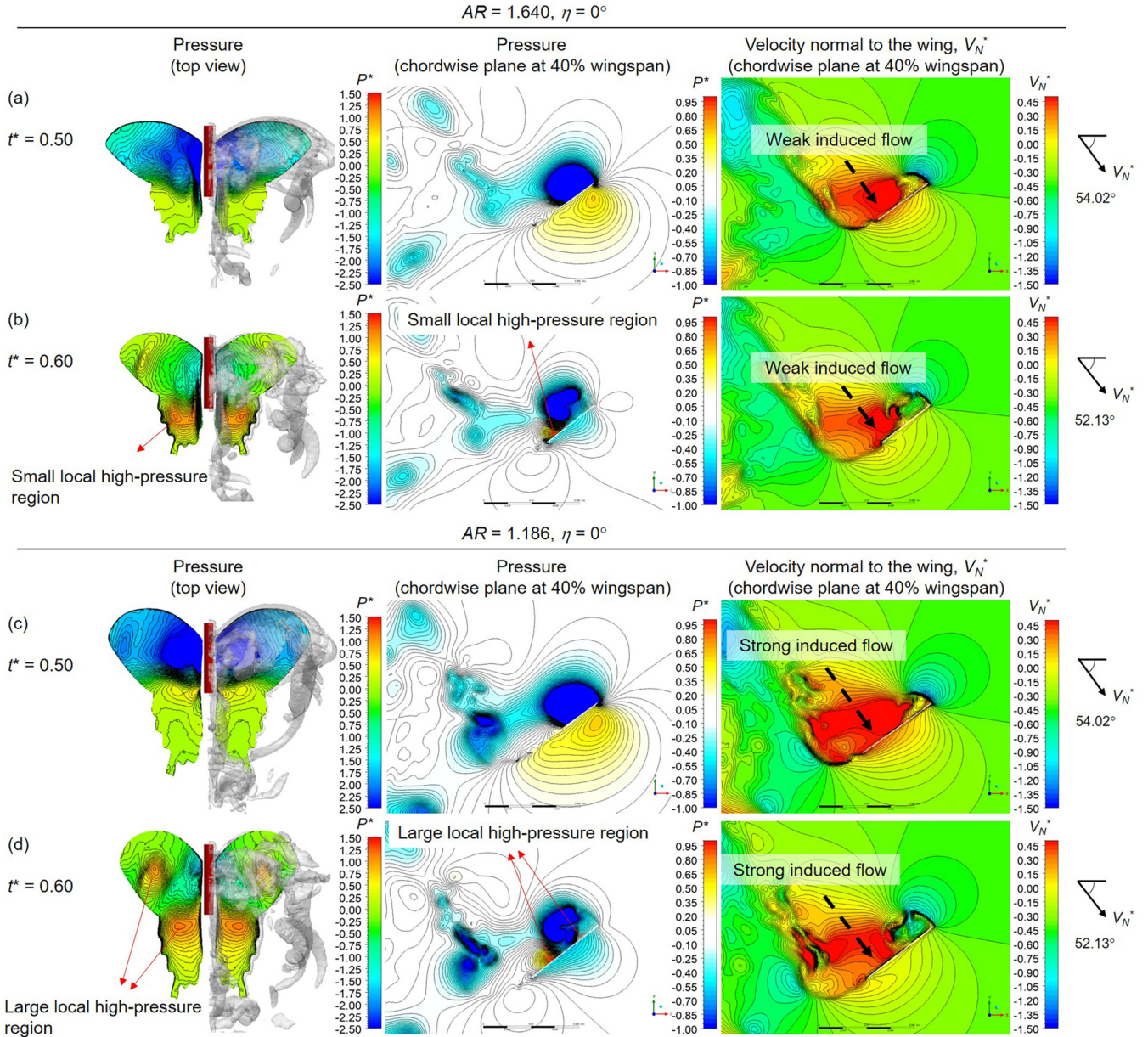
FIG. 12. Pressure and velocity contours of *Papilio polytes* in (a) and (b) AR = 1.640 and (c) and (d) AR = 1.186 at a wing-reversal stage. The vortex structure is identified with a Q criterion according to $Q = 40(2\Delta\phi f)^2$. The pressure is normalized with $P^* = P/[0.5\rho(2\Delta\phi f b)^2]$. The velocity normal to a wing is normalized with $V_N^* = V_N/(2\Delta\phi f b)$.

the instantaneous forces generated in the cycle. During the downstroke, the trends of instantaneous forces in *P. polytes* and *K. inachus* differ. For *P. polytes*, as η increases and AR decreases, the lift and drag in the downstroke decrease [Fig. 14(c)], but for *K. inachus*, the lift and drag in the downstroke increase [Fig. 14(d)]. The reason is that, when η varies from $-12.5°$ to $25°$, decreasing AR increases the strength of low pressure in the wake, but increasing η simultaneously decreases the strength of WTV and the spanwise flow speed [Figs. 15(a) and 15(b)]; coupling these effects, the LEV attachment diminishes in *P. polytes*, which makes the lift and drag in the downstroke decrease as η increases and AR decreases [Fig. 14(c)]. In contrast, for *K. inachus*, when η varies from $-12.5°$ to $25°$, AR decreases more (from 1.693 to

1.109, altered by -0.584) than that in *P. polytes* (from 1.640 to 1.186, altered by -0.424). Although the strength of WTV and the spanwise flow speed are decreased with increasing η, the more greatly decreased value of AR in *K. inachus* provides a much larger strength of low pressure in the wake [compare the pressure contours in Figs. 15(b) and 15(d)], which finally enhances the LEV attaching to the wing. The lift and drag in the downstroke in *K. inachus*, thereby, increase as η increases and AR decreases [Fig. 14(d)].

During an upstroke, the force trends in *P. polytes* and *K. inachus* are similar [Figs. 14(c) and 14(d)]. As η increases and AR decreases, the lift and drag in the upstroke decrease. The reason is that, in the upstroke, the effect of η is little (Sec. III A); the forces are dominated by the effect of
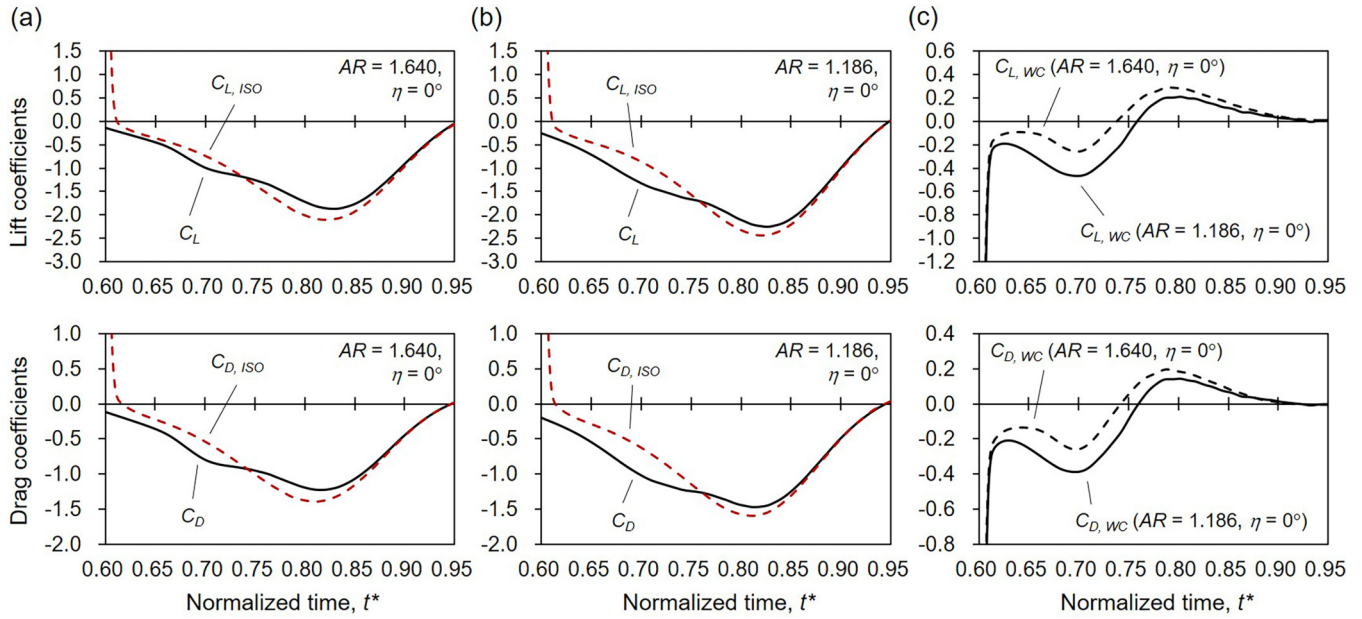
FIG. 13. Comparison of forces between the original simulation and the ISO simulation in (a) AR = 1.640 and $\eta = 0°$ and (b) AR = 1.186 and $\eta = 0°$. (c) Forces caused by the wake-capture effect.

AR. As AR decreases, the wake-capture effect is enhanced (Sec. III C). The lift and drag during the upstroke hence decrease as η increases and AR decreases.

Regarding lift-to-drag ratio, Figs. 14(a) and 14(b) show that, for both *P. polytes* and *K. inachus*, the maximum lift-to-drag ratio occurs at $\eta = 25°$ which minimizes AR. This result indicates that, in a flapping forward flight, sweeping a forewing forward relative to a hindwing (i.e., increasing η and decreasing AR) is suitable for cruising. In contrast, although a wing of small η with large AR has a smaller lift-to-drag ratio, the lift and drag are larger [Figs. 14(a) and 14(b)]; this suggests that sweeping a forewing backward is suitable for a flapping climbing flight. Ancel *et al.* [36], who investigated the effect of forewing-sweeping motion, obtained results opposite ours; they indicated that the maximum lift-to-drag ratio occurred at $\eta = 0°$ (in our definition) which maximized AR. The inconsistency between ours and theirs is due mainly to two reasons. First, according to the research in which the authors indicated that using the span-based Re is more appropriate to decouple the effect of AR from Re [14,27,28], in this paper, we adopted a constant span-based Re for analysis. The span-based Re in the study of Ancel *et al.* [36], in contrast, varied with the wing shape; the results might hence be altered by an effect of the varied span-based Re. Secondly, Ancel *et al.* [36] analyzed a steady gliding flight in which the wings were flattened and did not flap, whereas the wings and the body in this paper perform a flapping and a pitching motion, respectively, in which the transient mechanisms of the flapping wing are included. The study of Ancel *et al.* [36] is therefore applicable to a steady gliding flight with a combined effect of span-based Re. In contrast, with the isolation of the effect of span-based Re and the inclusion of the transient flow mechanisms, our results show that, in the flapping forward flight, the largest lift-to-drag ratio occurs at the largest wing-swept angle that minimizes the AR [Figs. 14(a) and 14(b)].

Although the trends of the mean forces and the lift-to-drag ratios are consistent in *P. polytes* and *K. inachus* [Figs. 14(a) and 14(b)], the force values at the same η and AR in these two butterflies differ, as shown in Fig. 5. We consider this is due to the differences of the forewing and hindwing geometries between these two butterfly species. As the wing of a butterfly consists of partially overlapping forewing and hindwing, the aerodynamic performance is affected by not only η and AR of the entire wing but also the individual geometries of the forewing and the hindwing. According to the research, butterflies (*Pararge aegeria*) with narrow and long forewings tend to have high taking-off accelerations [48], and the hindwing tail of a swallowtail butterfly (*Graphium policenes*) increases the lift and lift-to-drag ratio during gliding [49]. In this paper, compared with *K. inachus*, *P. polytes* has a narrower and longer forewing and a hindwing tail (Fig. 3). The geometrical differences of the forewing and hindwing between *P. polytes* and *K. inachus* may be a cause of the force value difference shown in Fig. 5.

In this paper, we used two butterfly species that have distinct forewing and hindwing geometries to investigate the effects of η and AR. We found that the effects of η and AR were decoupled; both have distinct flow mechanisms and aerodynamic force trends and are consistent in the two butterfly species (Secs. III A to III C). We also found that, for both butterfly species, the largest lift-to-drag ratio occurs at the largest η that minimizes AR [Figs. 14(a) and 14(b)]. The decoupling method and the results presented in this paper may provide a way to find a general wing configuration in butterfly flight and inspire an alternative design of a flapping MAV that utilizes the forewing-sweeping motion to control the wing shape and the flight.
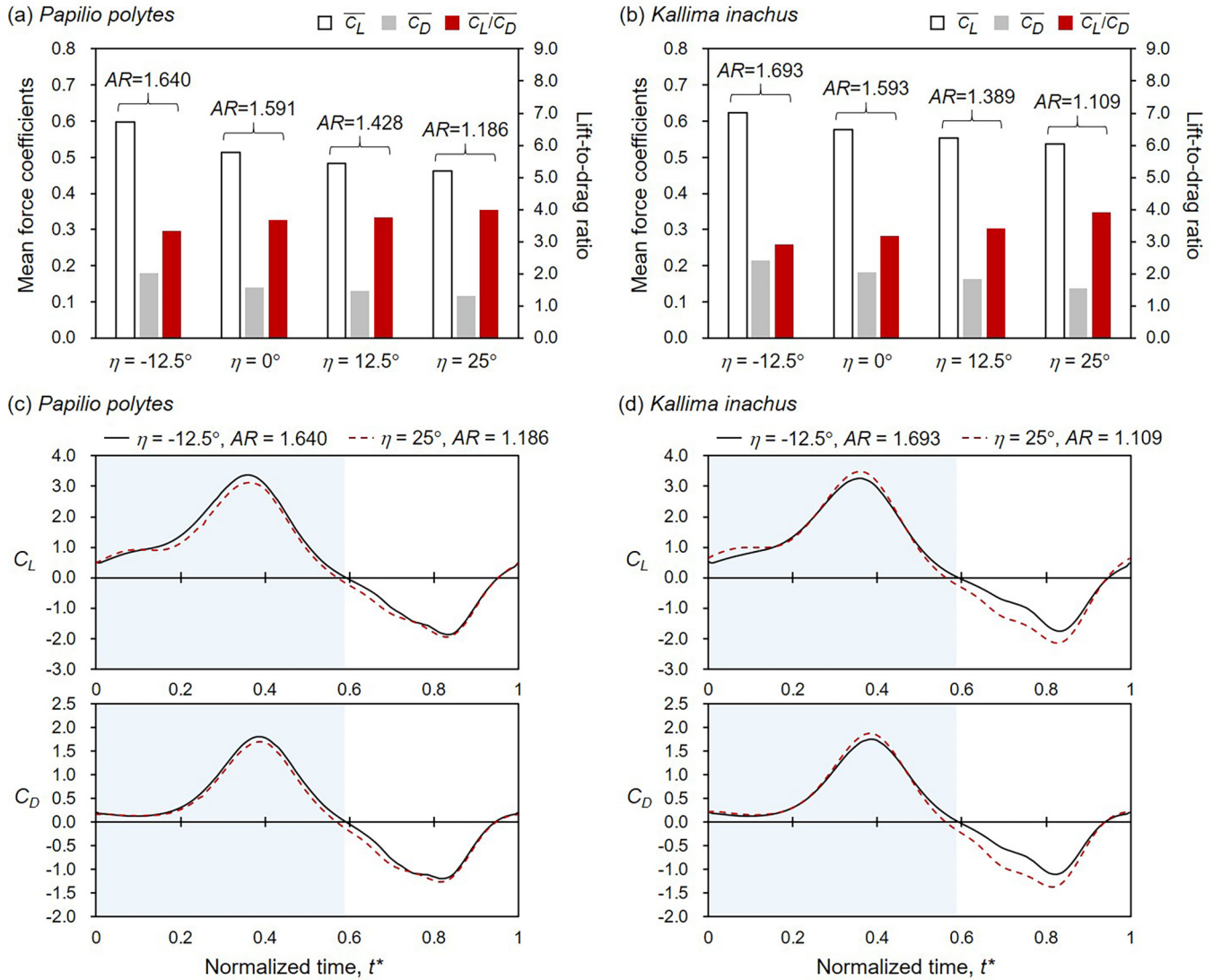
FIG. 14. Mean lift, drag coefficients, and lift-to-drag ratio over a flapping cycle in (a) *Papilio polytes* and (b) *Kallima inachus*. Instantaneous lift and drag coefficients in (c) *P. polytes* and (d) *K. inachus*.

IV. CONCLUSIONS

The objective of this paper was to clarify the decoupled effects of the wing-swept angle and AR on a forward-flying butterfly. Based on two butterfly species (*P. polytes* and *K. inachus*), we created a series of wing-shape models with varied combinations of η and AR and conducted numerical simulations for analysis. To decouple and compare the effects of the η and AR between these two butterfly species, we adopted the flying motion in the model as the average motion of the two butterfly species measured in the experiment; the span-based Reynolds number (Re = 3400) and the advance ratio ($J = 0.65$) were fixed.

Our results show that, through the wing models and the dimensionless method established in this paper, the effects of η and AR were decoupled. The aerodynamic force trends and flow mechanisms caused by η and AR are distinct but consistent in the two butterfly species. For fixed AR, as η decreases, the lift and drag during a downstroke increase and vary little in an upstroke. During the downstroke, a wing of

small η increases the strength of a WTV and the spanwise flow speed, which enhance the LEV attaching on the inboard wing surface and increase the lift and drag. Although a wing of large η has a LEV attachment on the outboard wing due to the inward spanwise flow caused by the upstream flow, the LEV detaches from most of the inboard wing, decreasing the lift and drag. For fixed η, as AR decreases, the lift and drag in a downstroke increase, and those in an upstroke decrease. During the downstroke, a wing of small AR induces a large region of low pressure in its wake, which promotes LEV to attach on the wing and increases the lift and drag; at a wing reversal stage, this large region of low pressure in its wake induces a strong flow toward the wing, so that the wake-capture effect is enhanced and increases the negative lift and negative drag in the upstroke. Over a flapping cycle, the mean lift and the mean drag increase as η decreases; the mean lift increases and the mean drag decreases as AR decreases.

On coupling the effects of the η and AR, we found that, for the two butterfly species, the mean lift and mean drag over a flapping cycle increase as η decreases and AR increases. The
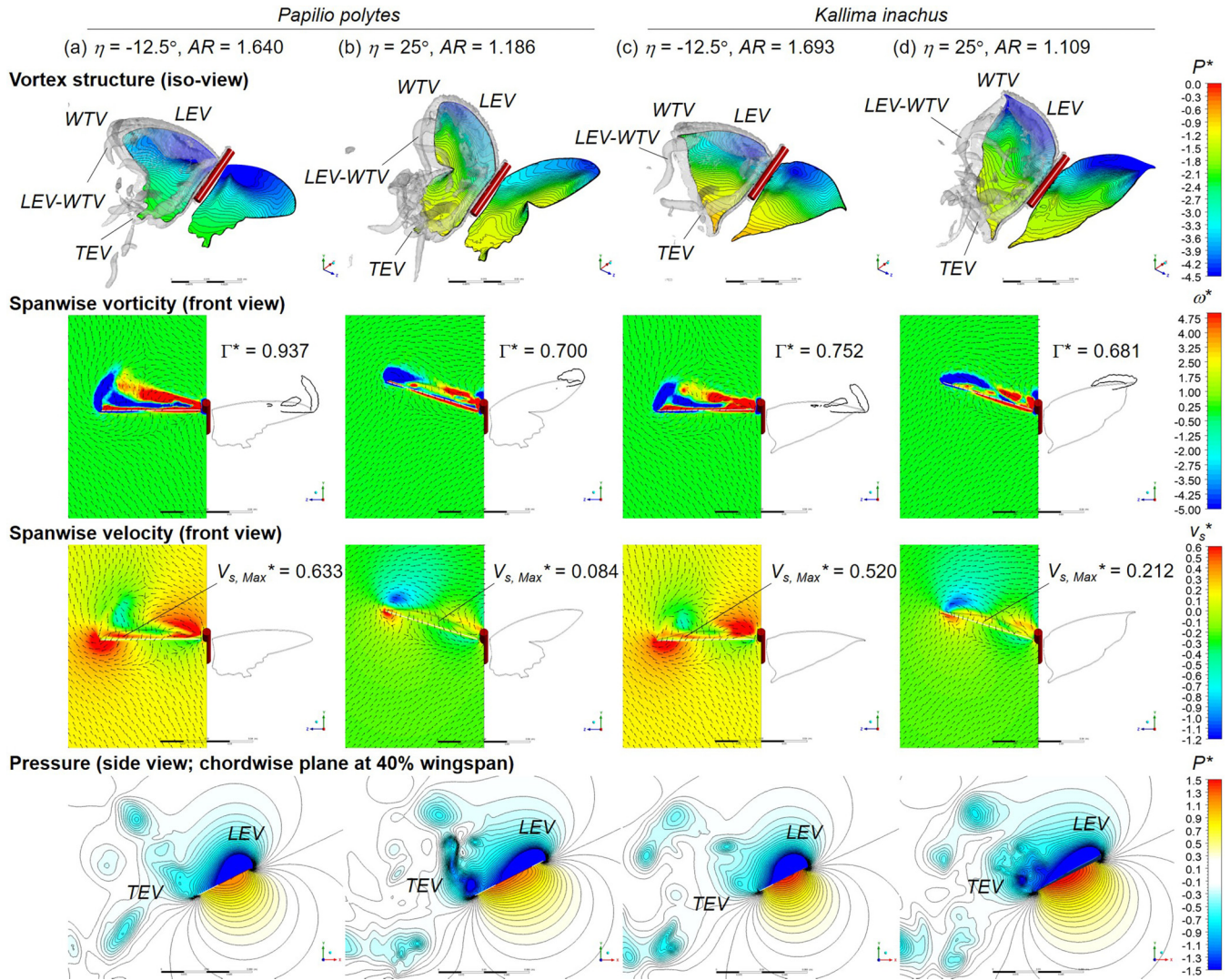
FIG. 15. Vortex structure, spanwise vorticity, spanwise velocity, and pressure contours in (a) and (b) *Papilio polytes* and (c) and (d) *Kallima inachus* with varied forewing-sweeping orientations. The vortex structure is identified with a Q criterion according to $Q = 40(2\Delta\phi f)^2$. The vorticity is normalized with $\omega^* = \omega/(2\Delta\phi f)$. The circulation is normalized with $\Gamma^* = \Gamma/(2\Delta\phi f b^2)$, in which the integral area is encompassed with a vorticity contour line of value $16\Delta\phi f$ (black lines near the wingtips). The spanwise velocity is normalized with $V_s^* = V_s/(2\Delta\phi f b)$. The pressure is normalized with $P^* = P/[0.5\rho(2\Delta\phi f b)^2]$.

largest lift-to-drag ratio occurs at the largest η that minimizes the AR. These conditions indicate that sweeping a forewing forward relative to a hindwing is suitable for cruising in a flapping forward flight, and sweeping a forewing backward relative to a hindwing is suitable for a flapping climbing flight. These results may inspire the design of a flapping MAV that uses the forewing-sweeping motion to control the wing shape and flight.

In this paper, we decoupled the wing-swept angle and AR based on the real wings of two butterfly species and analyzed and compared their decoupled and coupled effects. The decoupling method, flow mechanisms, and decoupled and coupled effects presented in this paper provide insight into the flight of a butterfly and the design of a MAV. However, some limitations should be noted. As discussed in the text, the wing of a butterfly consists of partially overlapping forewing and hindwing; the aerodynamic effect of wing shape is affected by not only η and AR of the entire wing but also the individual

geometries of the forewing and hindwing. The effects of forewing and hindwing geometries on flight need further clarification. In addition, the flight of a butterfly involves multiple factors such as transient flight velocity, wing motion, and body motion. In this paper, we focused on the flapping forward flight in which the forward-flight speed ($V = 1.177$ m s^{-1}), span-based Reynolds number (Re = 3400), advance ratio ($J = 0.65$), and the wing and body motions were fixed. The effects of wing shape on other flight modes need further clarification also.

[1] W. Shyy, H. Aono, C. K. Kang, and H. Liu, *An Introduction to Flapping Wing Aerodynamics* (Cambridge University Press, New York, 2013).

[2] Z. Terze, V. Pandža, M. Kasalo, and D. Zlatar, Discrete mechanics and optimal control optimization of flapping wing dynamics for Mars exploration, Aerosp. Sci. Technol. **106**, 106131 (2020).

[3] R. Dudley and R. B. Srygley, Flight physiology of neotropical butterflies: Allometry of airspeeds during natural free flight, J. Exp. Biol. **191**, 125 (1994).

[4] H. Tanaka and I. Shimoyama, Forward flight of swallowtail butterfly with simple flapping motion, Bioinspir. Biomim. **5**, 026003 (2010).

[5] K. Senda, T. Obara, M. Kitamura, N. Yokoyama, N. Hirai, and M. Iima, Effects of structural flexibility of wings in flapping flight of butterfly, Bioinspir. Biomim. **7**, 025002 (2012).

[6] K. C. Tejaswi, M. K. Sridhar, C. K. Kang, and T. Lee, Effects of abdomen undulation in energy consumption and stability for monarch butterfly, Bioinspir. Biomim. **16**, 046003 (2021).

[7] H. Huang and M. Sun, Forward flight of a model butterfly: Simulation by equations of motion coupled with the Navier-Stokes equations, Acta. Mech. Sin. **28**, 1590 (2012).

[8] Y. H. J. Fei and J. T. Yang, Enhanced thrust and speed revealed in the forward flight of a butterfly with transient body translation, Phys. Rev. E **92**, 033004 (2015).

[9] Y. H. J. Fei and J. T. Yang, Importance of body rotation during the flight of a butterfly, Phys. Rev. E **93**, 033124 (2016).

[10] A. T. Bode-Oke and H. Dong, The reverse flight of a monarch butterfly (*Danaus plexippus*) is characterized by a weight-supporting upstroke and postural changes, J. R. Soc. Interface **17**, 20200268 (2020).

[11] T. Fujikawa, Y. Sato, T. Yamashita, and K. Kikuchi, Development of a lead-lag mechanism using simple flexible links for a small butterfly-style flapping robot, 2010 World Automation Congress (2010), pp. 1–6.

[12] S. Sunada, K. Kawachi, I. Watanabe, and A. Azuma, Performance of a butterfly in take-off flight, J. Exp. Biol. **183**, 249 (1993).

[13] Y. Ozawa, T. Fujikawa, and K. Kikuchi, Analysis of turning motion for developing a butterfly-style flapping robot, MM Sci. J. **2018**, 2198 (2018).

[14] S. S. Bhat, J. Zhao, J. Sheridan, K. Hourigan, and M. C. Thompson, Uncoupling the effects of aspect ratio, Reynolds number and Rossby number on a rotating insect-wing planform, J. Fluid Mech. **859**, 921 (2019).

[15] K. Suzuki and M. Yoshino, A trapezoidal wing equivalent to a *Janatella leucodesma*'s wing in terms of aerodynamic performance in the flapping flight of a butterfly model, Bioinspir. Biomim. **14**, 036003 (2019).

[16] S. K. Chang, Y. H. Lai, Y. J. Lin, and J. T. Yang, Enhanced lift and thrust via the translational motion between the thorax-abdomen node and the center of mass of a butterfly with a constructive abdominal oscillation, Phys. Rev. E **102**, 062407 (2020).

[17] S. A. Ansari, K. Knowles, and R. Żbikowski, Insectlike flapping wings in the hover part 2: Effect of wing geometry, J. Aircr. **45**, 1976 (2008).

[18] A. Shahzad, F. B. Tian, J. Young, and J. C. S. Lai, Effects of wing shape, aspect ratio and deviation angle on aerody-

[19] namic performance of flapping wings in hover, Phys. Fluids **28**, 111901 (2016).

[19] J. S. Han, J. W. Chang, and H. K. Cho, Vortices behavior depending on the aspect ratio of an insect-like flapping wing in hover, Exp. Fluids **56**, 181 (2015).

[20] N. Phillips, K. Knowles, and R. J. Bomphrey, The effect of aspect ratio on the leading-edge vortex over an insect-like flapping wing, Bioinspir. Biomim. **10**, 056020 (2015).

[21] M. H. Dickinson, F. O. Lehmann, and S. P. Sane, Wing rotation and the aerodynamic basis of insect flight, Science **284**, 1954 (1999).

[22] J. W. Kruyt, G. F. van Heijst, D. L. Altshuler, and D. Lentink, Power reduction and the radial limit of stall delay in revolving wings of different aspect ratio, J. R. Soc. Interface **12**, 20150051 (2015).

[23] Y. J. Lee, K. B. Lua, and T. T. Lim, Aspect ratio effects on revolving wings with Rossby number consideration, Bioinspir. Biomim. **11**, 056013 (2016).

[24] G. Luo and M. Sun, The effects of corrugation and wing planform on the aerodynamic force production of sweeping model insect wings, Acta. Mech. Sin. **21**, 531 (2005).

[25] Z. R. Carr, A. C. DeVoria, and M. J. Ringuette, Aspect-ratio effects on rotating wings: Circulation and forces, J. Fluid Mech. **767**, 497 (2015).

[26] D. J. Garmann and M. R. Visbal, Dynamics of revolving wings for various aspect ratios, J. Fluid Mech. **748**, 932 (2014).

[27] R. R. Harbig, J. Sheridan, and M. C. Thompson, Reynolds number and aspect ratio effects on the leading-edge vortex for rotating insect wing planforms, J. Fluid Mech. **717**, 166 (2013).

[28] S. S. Bhat, J. Zhao, J. Sheridan, K. Hourigan, and M. C. Thompson, Aspect ratio studies on insect wings, Phys. Fluids **31**, 121301 (2019).

[29] T. Fujikawa, Y. Sato, Y. Makata, T. Yamashita, and K. Kikuchi, Motion analysis of butterfly-style flapping robot for different wing and body design, in *Proceedings of the 2008 IEEE International Conference on Robotics and Biomimetics* (IEEE, New York, 2009), pp. 216–221.

[30] J. Jayakumar, K. Senda, and N. Yokoyama, Control of pitch attitude by abdomen during forward flight of two-dimensional butterfly, J. Aircr. **55**, 2327 (2018).

[31] C. P. Ellington, C. van den Berg, A. P. Willmott, and A. L. R. Thomas, Leading-edge vortices in insect flight, Nature (London) **384**, 626 (1996).

[32] J. M. Birch and M. H. Dickinson, Spanwise flow and the attachment of the leading-edge vortex on insect wings, Nature (London) **412**, 729 (2001).

[33] D. Lentink and M. H. Dickinson, Rotational accelerations stabilize leading edge vortices on revolving fly wings, J. Exp. Biol. **212**, 2705 (2009).

[34] T. Jardin and L. David, Spanwise gradients in flow speed help stabilize leading-edge vortices on revolving wings, Phys. Rev. E **90**, 013011 (2014).

[35] T. Jardin and L. David, Coriolis effects enhance lift on revolving wings, Phys. Rev. E **91**, 031001(R) (2015).

[36] A. O. Ancel, R. Eastwood, D. Vogt, C. Ithier, M. Smith, R. Wood, and M. Kovač, Aerodynamic evaluation of wing shape and wing orientation in four butterfly species using numerical simulations and a low-speed wind tunnel, and its implications for the design of flying micro-robots, Interface Focus **7**, 20160087 (2016).

[37] P. Y. Zou, Y. H. Lai, and J. T. Yang, Effects of phase lag on the hovering flight of damselfly and dragonfly, Phys. Rev. E **100**, 063102 (2019).

[38] Y. H. Lai, Y. J. Lin, S. K. Chang, and J. T. Yang, Effect of wing-wing interaction coupled with morphology and kinematic features of damselflies, Bioinspir. Biomim. **16**, 016017 (2020).

[39] Y. H. Lai, J. F. Ma, and J. T. Yang, Flight maneuver of a damselfly with phase modulation of the wings, Integr. Comp. Biol. **61**, 20 (2021).

[40] Y. J. Lin, S. K. Chang, Y. H. Lai, and J. T. Yang, Beneficial wake-capture effect for forward propulsion with a restrained wing-pitch motion of a butterfly, R. Soc. Open Sci. **8**, 202172 (2021).

[41] B. Liang and M. Sun, Aerodynamic interactions between wing and body of a model insect in forward flight and maneuvers, J. Bionic Eng. **10**, 19 (2013).

[42] X. Yu and M. Sun, A computational study of the wing-wing and wing-body interactions of a model insect, Acta. Mech. Sin. **25**, 421 (2009).

[43] K. Suzuki, T. Aoki, and M. Yoshino, Effect of chordwise wing flexibility on flapping flight of a butterfly model using immersed-boundary lattice Boltzmann simulations, Phys. Rev. E **100**, 013104 (2019).

[44] K. Suzuki, K. Minami, and T. Inamuro, Lift and thrust generation by a butterfly-like flapping wing-body model: Immersed boundary-lattice Boltzmann simulations, J. Fluid Mech. **767**, 659 (2015).

[45] K. B. Lua, T. T. Lim, and K. S. Yeo, Effect of wing-wake interaction on aerodynamic force generation on a 2D flapping wing, Exp. Fluids **51**, 177 (2011).

[46] Y. J. Lee and K. B. Lua, Wing-wake interaction: Comparison of 2D and 3D flapping wings in hover flight, Bioinspir. Biomim. **13**, 066003 (2018).

[47] F. O. Lehmann, When wings touch wakes: Understanding locomotor force control by wake-wing interference in insect wings, J. Exp. Biol. **211**, 224 (2007).

[48] K. Berwaerts, E. Matthysen, and H. Van Dyck, Take-off flight performance in the butterfly *Pararge aegeria* relative to sex and morphology: A quantitative genetic assessment, Evol.: Intl. J. Org. Evol. **62**, 2525 (2008).

[49] H. Park, K. Bae, B. Lee, W. P. Jeon, and H. Choi, Aerodynamic performance of a gliding swallowtail butterfly wing model, Exp. Mech. **50**, 1313 (2010).